

Experiments on Flapping Flight under Hovering condition

A Thesis
Submitted for the Degree of
MASTER OF SCIENCE (ENGINEERING)

by

NAKUL PANDE



ENGINEERING MECHANICS UNIT
JAWAHARLAL NEHRU CENTRE FOR ADVANCED SCIENTIFIC
RESEARCH
(A Deemed University)
Bangalore – 560 064

JULY 2016

DECLARATION

I hereby declare that the matter embodied in the thesis entitled “**Experiments on flapping flight under Hovering condition**” is the result of investigations carried out by me at the Engineering Mechanics Unit, Jawaharlal Nehru Centre for Advanced Scientific Research, Bangalore, India under the supervision of Prof. K. R. Sreenivas and that it has not been submitted elsewhere for the award of any degree or diploma.

In keeping with the general practice in reporting scientific observations, due acknowledgment has been made whenever the work described is based on the findings of other investigators.

Nakul Pande

CERTIFICATE

I hereby certify that the matter embodied in this thesis entitled “**Experiments on flapping flight under Hovering condition**” has been carried out by Mr. Nakul Pande at the Engineering Mechanics Unit, Jawaharlal Nehru Centre for Advanced Scientific Research, Bangalore, India under my supervision and that it has not been submitted elsewhere for the award of any degree or diploma.

Prof. K. R. Sreenivas (Research Supervisor)

ACKNOWLEDGEMENT

My research supervisor Professor KR Sreenivas has helped me a lot in the work that I have done here. Fresh after leaving my job, he gave me the opportunity to work in his lab. He has always been approachable, and patient with the many doubts that I have had. Most of all I would like to thank him for the freedom that he has given me while working in this project.

The courses that I have taken in JNC have helped me approach the problem better. Also, Siddharth, Shashank and my other lab-mates have always been open to having a discussion about my work. I am grateful for that.

Finally I would like to thank my family for supporting me in all my decisions

TABLE OF CONTENTS

| | Page |
|--|-------------|
| ABSTRACT..... | v |
| LIST OF FIGURES..... | vi |
| CHAPTER 1: INTRODUCTION | |
| 1.1 Introduction..... | 1 |
| 1.2 Literature Review..... | 2 |
| 1.3 Motivation..... | 5 |
| CHAPTER 2: EXPERIMENTS | |
| 2.1 Experimental Setup..... | 8 |
| 2.2 Flapping Motion..... | 12 |
| 2.2.1 Tracking the Wing Motion..... | 13 |
| 2.2.2 Repeatability of Wing Motion..... | 15 |
| 2.3 Particle Image Velocimetry..... | 17 |
| 2.3.1 Repeatability of PIV..... | 18 |
| 2.4 Experimental Conditions and Non-Dimensional Numbers..... | 22 |
| 2.5 Seeding Density..... | 24 |
| CHAPTER 3: RESULTS I: QUALITATIVE OBSERVATIONS | |
| 3.1 “Two-jet” or “Four-jet”..... | 26 |
| 3.2 “Jet Meandering”..... | 28 |
| 3.3 3D effects..... | 30 |
| CHAPTER 4: RESULTS II: FORCE CALCULATION | |
| 4.1 General Control Volume analysis | 34 |
| 4.2 Control Volume analysis for this problem..... | 36 |
| 4.3 Lift Calculation Details..... | 41 |
| 4.4 Lift variation across flapping cycles..... | 42 |
| 4.5 Assessment and validity of the lift calculation..... | 45 |

| | | |
|-----|--|----|
| 4.6 | Comparison across Reynolds Number..... | 47 |
| 4.7 | Comparison across all Experiments and with 2D simulations..... | 48 |
| 4.8 | A note on instantaneous forces..... | 50 |

CHAPTER 5: CONCLUSION AND FUTURE WORK

| | | |
|-----|------------------|----|
| 5.1 | Conclusion..... | 56 |
| 5.2 | Future work..... | 57 |

| | | |
|-------------------|--|----|
| Appendix 1 | | 58 |
|-------------------|--|----|

| | | |
|-------------------|--|----|
| Appendix 2 | | 59 |
|-------------------|--|----|

| | | |
|-------------------|--|----|
| Appendix 3 | | 61 |
|-------------------|--|----|

| | | |
|---------------------------|--|----|
| LIST OF REFERENCES | | 62 |
|---------------------------|--|----|

ABSTRACT

In the recent past, we have begun to recognize many of the benefits that Micro Air Vehicles (MAV's) may have. The important ones being, their small size and high manoeuvrability, which makes them suitable for reconnaissance, exploration, and even, targeted payload delivery. In this backdrop, unsteady flight has received considerable attention. Many unsteady mechanisms have been proposed that can be used for generating sustained lift. One such mechanism that could be used for MAV application is asymmetric flapping. Asymmetric flapping is a simple wing kinematics in which downward stroke is faster than the upward stroke. This thesis aims to understand the role of asymmetric flapping in hovering flight. A one degree of freedom flapping model is designed and asymmetry is introduced by making the downstroke faster than the upstroke, while keeping the total flapping time-period constant. Work done in our group previously using two-dimensional numerical simulations and flow visualization experiments, has found an optimum asymmetry ratio, for which maximum lift is obtained. With a view to quantify these findings with experiments, a range of asymmetry ratios (ratio of downstroke time to upstroke time) is studied using two-dimensional PIV. For this, a mechanical model is used with a fixed aspect ratio, flapping amplitude and velocity profile. Typical Reynolds number used in the present study is about three hundred.

Some of the results from the present study are mentioned here. We observe that the flow-field meanders, and doesn't reach a steady-state configuration. This has been seen in the past in the context of modelling fish propulsion studies. With increasing asymmetry (decreasing asymmetry ratio) of wing motion, however, the flow aligns in the direction of the faster stroke. Contrary to earlier studies, we noticed that three-dimensional effects are prominent and significantly affect the flow as well. Using the velocity field obtained using PIV, lift forces are estimated using a control volume approach. It is found that the average lift force increases monotonously with increasing flapping asymmetry (that is decreasing asymmetry ratio) and that there is no optimum maximum. Furthermore, a transient peak is observed in the lift force which should be addressed while designing MAV's. Drag for an impulsively started cylinder shows a similar behaviour, and the two have been compared here. Finally, the flow and forces derived are also used to corroborate 3D numerical simulations done in our group.

LIST OF FIGURES

The nomenclature of figures goes as: *Chapter. FigureNumber*

| Figure | Title | Page |
|--------|--|------|
| 1.1 | Variation of flapping frequency of birds with their wing-size. Adopted from (Dhawan, 1991), reproduced from (Shreyas, Devranjan, & Sreenivas, Aerodynamics of Bird and Insect flight, 2011) | 1 |
| 1.2 | Clap and Fling (Weis Fogh, 1973). The wings ‘clap’ together at the end of the upstroke and the leading edges ‘fling’ apart at the beginning of the downstroke, as described originally by Weis Fogh | 2 |
| 1.3 | Flow and forces for a 2D impulsively started ellipse with aspect ratio $1/8$, $Re = 1000$ (based on free stream velocity, u_0), and, angle of attack 40° . Non-dimensional convective time: $t_s = tu_0/\text{chord}$. Region A: is due to the impulsive start. Region B: corresponds to the rollup of the vortex sheet near the tips of the ellipse. Region C: shows a temporary plateau in the force before the leading edge vortex is shed, and Region D: shows the periodic force associated with the von Karman wake (Wang, 2000) | 3 |
| 1.4 | Streak photography of aluminium particles on surface for (a) symmetric flapping ($t_U=10s$, $t_D=10s$) typical Reynolds number ~ 1000 , and, (b) asymmetric flapping ($t_U=20s$, $t_D=10s$) typical Reynolds number ~ 670 . Wing aspect ratio = 6.25, therefore it is almost 2D (Shreyas, 2005) | 6 |
| 1.5 | Result of 2D discrete vortex simulations. 45 rev/s corresponds to $Re \sim 1200$ (Other values of Re increase linearly with increase in frequency of flapping). Amplitude of flapping = 80° , mean position of wing = -20° , wing length = 1 cm (Devranjan, 2009) | 7 |
| 2.1 | Schematic of flapping mechanism as well as photo of the drive assembly with timing pulley and spur gears. | 9 |
| 2.2 | Schematic of Experimental Setup | 10 |
| 2.3 | Photograph of Experimental Setup | 11 |
| 2.4 | Theoretical velocity profile over a cycle or the velocity profile programmed into controller (Blue: AR 1 to Red: AR 0.6) | 12 |

| | | |
|------|--|----------|
| 2.5 | (a) shows a schematic to give an idea of how theta is measured with respect to the wing. (b) Presents the theoretical theta (angular position) profile over a cycle, as a result of the programmed velocity profile. (Blue: AR 1 to Red: AR 0.6) | 12,13 |
| 2.6 | Example of actual theta profile over a cycle extracted from experimental images: 200 frames per cycle, Image recording frequency. (Blue: AR 1 to Red: AR 0.6) | 14 |
| 2.7 | Actual theta profile over a cycle extracted from experimental images (200 frames per cycle) for different sets of experiments, $Re = 314$, (a) $AR = 1$, (b) $AR = 0.9$, (c) $AR = 0.8$, (d) $AR = 0.7$ | 15 |
| 2.8 | Example of instantaneous streaks and corresponding velocity and vorticity fields for $Re = 628$, $AR = 0.6$. The colour represents vorticity, and the axis has been suitably chosen to show comparison with streaks | 17 |
| 2.9 | Velocity and vorticity fields for 2 different experiments (two-wings) $Re = 314$, $AR = 1$, at the end of different cycles (a)-(d). | 18,19,20 |
| 2.10 | Velocity and vorticity fields for 2 different experiments (one-wing) $Re = 314$, $AR = 1$, at end of different cycles (a)-(d). Horizontal scale: 0 - 3.5, Vertical scale: 0 - 6.5. Vorticity values have been normalized with the Time-Period of flapping; the colour bar is as show. All the velocity-vorticity plots shown henceforth, therefore, have the same horizontal-vertical extent and the same vorticity scale. | 20,21 |
| 2.11 | Example images showing seeding density for all the sets of experiments done | 24,25 |
| 3.1 | Instantaneous velocity and vorticity field $Re=314$, for (a) symmetric flapping ($AR = 1$), and (b) asymmetric flapping ($AR = 0.7$). Both plots, (a) and (b) have been obtained for the same wing. The left and right images in figure (a) and (b) are just mirror copies of each other and present the typical flow field. | 26,27 |
| 3.2 | Instantaneous velocity and vorticity field $Re=314$, for symmetric flapping at different flapping-cycle times. See figure 2.10 for the corresponding vorticity scale. | 28 |
| 3.3 | Instantaneous velocity and vorticity field $Re=314$, for asymmetric flapping ($AR = 0.7$) at different flapping-cycle times. Same vorticity | 29 |

| | | |
|-----|--|----------|
| | scale as figure 3.2 | |
| 3.4 | Comparison of instantaneous velocity-vorticity and velocity-source field, $Re=314$, for symmetric flapping during 1 st flapping cycle ($t = 0.5T$ to $t = T$). The source term has also been normalized with the Time-Period of flapping and has the same scale as vorticity shown in figure 3.5 | 30,31 |
| 3.5 | Comparison of instantaneous velocity-vorticity and velocity-source field, $Re=314$, for symmetric flapping during 2 nd flapping cycle ($t = T$ to $t = 1.5T$) | 31,32 |
| 3.6 | Schematic for origin of the source term in the mid-plane. Because of the finite size of the wing, the tip vortices formed will create an outward flow in the mid-plane of the wing | 33 |
| 4.1 | Schematic diagram used, to calculate force on a solid body, by the surrounding fluid, using control volume method | 34 |
| 4.2 | Schematic diagram used, to calculate force on a solid flapping body, by the surrounding fluid, using control volume method | 36 |
| 4.3 | Schematic diagram of one-wing and the velocity vectors obtained for the middle cross-section. | 38 |
| 4.4 | Schematic diagram of the flapping body. Forward-backward symmetry breaking has been observed previously in cases with just up-down flapping (Vandenbergh, Zhang, & Childress, 2004) | 39 |
| 4.5 | Example photo showing control volume overlaid on the PIV image in the present scenario (blue arrows show the showing 2 nd term in the above equation) | 40 |
| 4.6 | Variation of normalized lift on one wing ($Lift / (\frac{1}{2} \rho u_{tip}^2 span)$) vs AR for $Re = 314$; contribution of in-plane momentum flux (stars) against total normalized lift (dots) | 41 |
| 4.7 | Variation of average normalized in-plane momentum flux for one wing (each point corresponds to average value of lift until that point) over time, for $Re = 314$, (a) $AR=0.9$, (b) $AR=0.6$ for different experiments (each colour represents different runs) | 42 |
| 4.8 | Variation of instantaneous normalized in-plane momentum flux for one wing over time, across different experiments done, for $Re = 314$, (a) | 43,44,45 |

| | | |
|------|--|----|
| | AR =1, (b) AR =0.9, (c) AR =0.8, (d) AR =0.7 | |
| 4.9 | Schematic of in-plane meandering (left) and out-of-plane flow (right) | 46 |
| 4.10 | Variation normalized lift (for one-wing) vs AR, for different Re; Re = 314 (blue), Re = 628 (red) | 47 |
| 4.11 | Variation of normalized lift (for one wing) vs AR, Re 314; error-bar gives the variation across different realizations. For details of PIV of all the sets of experiments done refer to section 2.4 | 48 |
| 4.12 | Variation of normalized lift vs AR, 2D Discrete Vortex simulations. Data taken from (Devranjan, 2009) | 49 |
| 4.13 | Variation of instantaneous normalized acceleration term for one wing over time. Re 314, AR 0.7 | 50 |
| 4.14 | Variation of instantaneous normalized force (blue), calculated for one wing (for the mid-plane), and angular velocity (red) for one conditionally averaged cycle. Positive angular velocity represents downstroke. Re 314: AR 0.7 | 51 |
| 4.15 | Streamline time history (non-dimensional convective time: $T = \frac{U_0 t}{D}$) and evolution of drag force for an impulsively started cylinder (Koumoutsakos & Leonard, 1995). The pressure drag contribution (the shape and magnitude of which is almost the same as total drag) in particular is the one that can be compared directly with the present case. | 53 |
| 4.16 | Variation of instantaneous normalized force calculated for one wing (for the mid-plane) for one conditionally averaged cycle. Re 314: AR 0.7 (blue) and AR 0.9 (red) | 54 |
| 4.17 | Variation of instantaneous normalized force (blue) from 3D lattice Boltzmann simulations (Siddharth, 2016). Positive angular velocity represents downstroke. Re 314: AR 0.7 | 55 |
| 5.1 | Change in angular position of wing in <i>Diptera</i> showing asymmetric flapping strokes (minimum around $t= 0.4$). Adopted from Ennos (Ennos, 1989) | 56 |
| 5.2 | Wing motion of a painted stork in flight (The numbers represent the time in milliseconds taken to complete each stroke). Reproduced from (Shreyas, Devranjan, & Sreenivas, Aerodynamics of Bird and Insect flight, 2011). Adopted from (Dhawan, 1991) | 57 |

Chapter 1

INTRODUCTION

1.1 Introduction

When one thinks of flapping flight, what comes to mind immediately are examples in nature. From vultures and eagles, to the smallest of insects, flapping of wings is used ubiquitously by animals to keep themselves aloft. But looking closely what can be observed is that birds like eagles and vultures flap their wings only rarely, and glide and soar for most of their air-time. On the other hand small insects and birds (humming birds, house flies) move their wings much faster. Figure 1.1 shows how the wing beat rate varies with changing wing length of animals in nature.

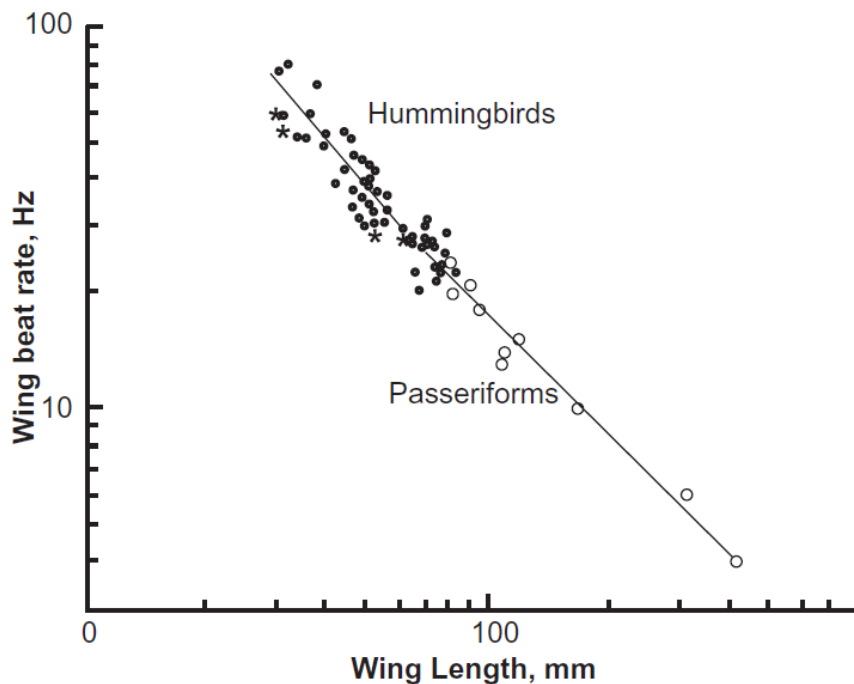


Figure 1.1: Variation of flapping frequency of birds with their wing-size. Adopted from (Dhawan, 1991), reproduced from (Shreyas, Devranjan, & Sreenivas, Aerodynamics of Bird and Insect flight, 2011)

This reveals that while large birds use steady aerodynamic principles for most of their flight, smaller animals have a wing-beat frequency of ~ 100 Hz, and must use very different unsteady aerodynamic mechanisms! (Shreyas, Devranjan, & Sreenivas, Aerodynamics of Bird and Insect flight, 2011)

1.2 Literature Review

Recently research in unsteady flight mechanisms has received impetus, primarily because of the need to design Micro-Air Vehicles (MAV's). To that end, the most common view has been to understand and mimic nature. Hence, many unsteady mechanisms used by birds and insects that have been under study for the past several decades, have been isolated and understood now.

The following summarizes them briefly.

- *Clap and Fling*: was first observed by Weis Fogh in the chalcid wasp *Encarsia formosa* (Weis Fogh, 1973). During the clap phase, the dorsal surface of the wings comes as shown in figure 1.2. More often, the leading edges meet first, which ensures that the air in between the wings is pushed downward, thereby providing lift to the insect. On the other hand during the 'fling' phase the leading edges peel apart while the trailing edges are still together. This creates a low pressure on the dorsal surface of the wing, which again, leads to an upward force.

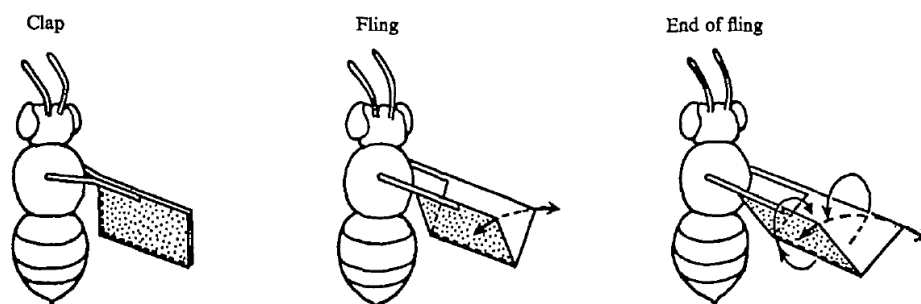


Figure 1.2: Clap and Fling (Weis Fogh, 1973). The wings 'clap' together at the end of the upstroke and the leading edges 'fling' apart at the beginning of the downstroke, as described originally by Weis Fogh (reproduced with permission)

Although most tiny insects use this mechanism, the majority of the insects do not (Miller & Peskin, 2005). It is therefore unlikely to provide a general explanation of flapping flight in insects. The advantage of this mechanism is that the lift generation is instantaneous (Shreyas, Devranjan, & Sreenivas, Aerodynamics of Bird and Insect flight, 2011)

- *Unsteady motion and delayed stall:* If an airfoil undergoes steady motion at high angles of attack, flow separation stalls the airfoil and it loses its lift. If however, the airfoil is set into motion abruptly, above its steady-state stalling angle, the airfoil can travel several lengths before stall occurs. Figure 1.3 shows the lift forces for a similar problem: simulation of the towing of an ellipse (Wang, 2000).

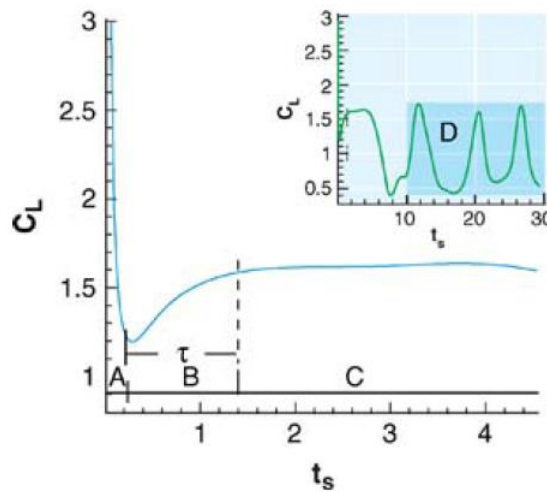


Figure 1.3: Forces for a 2D impulsively started ellipse with aspect ratio 1/8, $Re = 1000$ (based on free stream velocity, u_0), and, angle of attack 40° (reproduced with permission). Non-dimensional convective time: $t_s = tu_0/chord$. Region A: is due to the impulsive start. Region B: corresponds to the rollup of the vortex sheet near the tips of the ellipse. Region C: shows a temporary plateau in the force before the leading edge vortex is shed, and Region D: shows the periodic force associated with the von Karman wake (Wang, 2000)

Lift force remains reasonably high ($C_L \sim 1.5$) for up to 4 chord lengths of travel. Wang argues that the relevant time-scale for insect flapping is the characteristic time

in Region B: τ , which is of order one¹. It is only much later then, that lift forces drop, and become unsteady further on, due to the beginning of a von Karman wake. Furthermore, it has been seen in experiments (Birch & Dickinson, 2001) that the leading edge vortex (responsible for creating low pressure on top of the wing) remains stably attached for longer times for a 3D flapping wing than a simple 2D translating airfoil. A combination of these is observed to be used by insects hovering with a figure-of-8 wing motion.

- *Wing Rotation and wake capture:* At the end of each downstroke or upstroke, the insect wing is seen to rotate rapidly, such that the same edge of the wing faces the oncoming flow. This was observed to augment the lift force at stroke reversal in dynamically scaled experiments done by Dickinson et al (Dickinson, Lehmann, & Sane, 1999). Using the same experiments it was also found that, as the wing reverses direction, it encounters the enhanced velocity and acceleration fields due to recently shed wake, thus resulting in higher aerodynamic forces immediately following stroke reversal as well (Sane, 2003). This has been called wake capture or wing-wake interaction
- *Heaving and flapping in free stream/ reverse von Karman vortex-street:* When an airfoil (kept in a steady free-stream flow) is oscillated at sufficiently high amplitude and frequency, thrust is produced and a jet-like time-averaged axial velocity profile is observed in the wake (Heathcote & Gursul, 2007). The wake therefore changes from a von Karman vortex street to a reverse Benard-von Karman vortex street as the Strouhal number (non-dimensional frequency) is increased. Although this mechanism has usually been related to fish swimming, it can be used to understand forward flapping flight of birds.

Most of the mechanisms of generating lift described above, use complex wing kinematics of insect flight, like wing rotation, varying angle of attack etc. during flight. Therefore MAV's designed by reproducing insect like motion, will be elaborate, and the complexity will

¹ A similar trend in forces (Region A, B and C) is seen in this problem as well and is discussed in detail in section 4.9

increase the weight and reduce load carried by the MAV. The approach presented in this work, hence, is driven by the need of a simple engineering design.

Before proceeding further, it is important to note that as a broad classification, one can think of two modes of flapping flight:

- Forward Flight: The flapping motion is used to keep animal aloft, as well as to move forward. The animal uses the kinetic energy of the oncoming air combined with its own flapping wings, to provide the necessary lift and thrust.
- Hovering: It is an extreme mode of flight. The flapping motion is used to draw in the surrounding air from the ambient and provide a net downward momentum to the fluid (Wang, 2005), so that the animal can stay aloft (no thrust).

Hovering in nature, particularly, has been looked at in great detail, since:

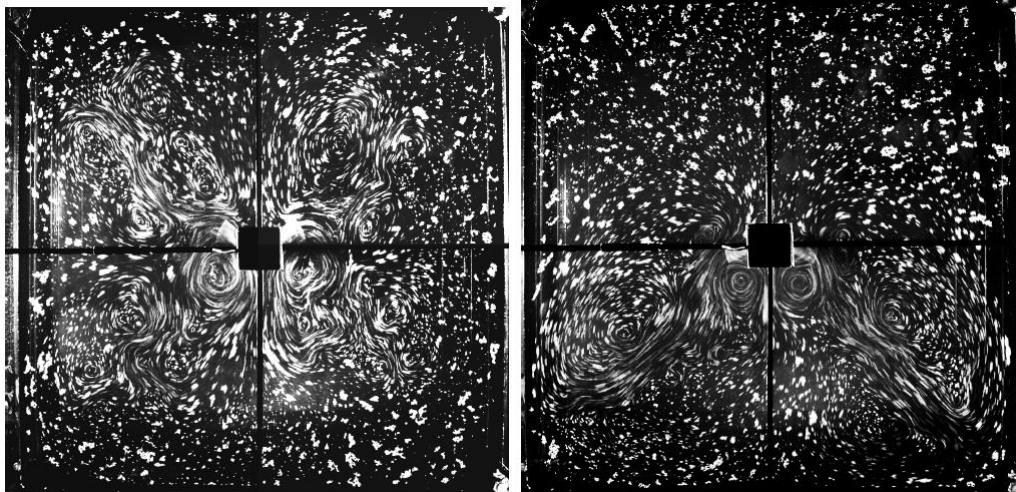
- For scientists: it is convenient to calculate the force balance by equating lift and weight in this case (Sane, 2003).
- For engineers: From the point of view of design of micro air-vehicles (autonomous tiny flying vehicles), if all flight and energy requirements are satisfied for this "extreme mode of flight", it is automatically satisfied for forward flight as well. In other words, if there is an MAV with a battery pack that can provide enough energy for it to sustain itself in air (hover), then, it can fly forward as well.

Keeping this in mind, the work described hence on has been conducted for the hovering flight scenario. Our research is aimed at looking at the simplest ways to creating asymmetry in the flow around the wing, such that it can be used, as a first step, for hovering flight.

1.3 Motivation

Asymmetric flapping is an unsteady mechanism that has been proposed by Sreenivas et al (Shreyas, Devranjan, & Sreenivas, Aerodynamics of Bird and Insect flight, 2011) as a way of producing lift. They conducted flow visualization experiments on a 1 degree-of-freedom, up-down flapping model whose motion was restrained otherwise (hovering). They observed, that if the down-stroke is faster (down-stroke time, t_D is lesser) than the up-stroke (up-stroke time,

t_U is more), there is a net downward momentum imparted to the fluid. They defined an asymmetry ratio, $AR = \frac{t_D}{t_U}$ for their experiments, such that symmetric flapping corresponds to $AR = 1$ (a counter-intuitive convention that unfortunately has been followed in this thesis)



(a) Symmetric Flapping

(b) Asymmetric Flapping

Figure 1.4: Streak photography of aluminium particles on surface for (a) symmetric flapping ($t_U=10s$, $t_D=10s$) typical Reynolds number ~ 1000 , and, (b) asymmetric flapping ($t_U=20s$, $t_D=10s$) typical Reynolds number ~ 670 . Wing aspect ratio = 6.25, therefore it is almost 2D (Shreyas, 2005)

The flow field switches from a four-jet (symmetric) to a two-jet (asymmetric) configuration when this stroke-time ratio (AR) is below a critical value. Figure 1.4 shows that symmetric flapping creates a jet in each of the four quadrants (four-jet), while asymmetric flapping does so only in the two lower quadrants, in the downward direction (two-jet). Even though the average Reynolds number (based on the average tip speed) is less in the case of asymmetric flapping (which results in a weaker jets compared to symmetric flapping), it can be deduced that it gives more lift than its symmetric counterpart shown here.

2D-discrete vortex simulations done later in our group also gave insight into the problem (Devranjan, 2009). They indicated, as shown in figure 1.5, for certain flapping frequencies the optimal value of the asymmetry ratio, for getting maximum lift, was found to be around

0.7. It should be noted though, that there is no clear maxima seen for lower $Re \sim 1200$ (45 Hz), for which case the variation is erratic with many peaks.

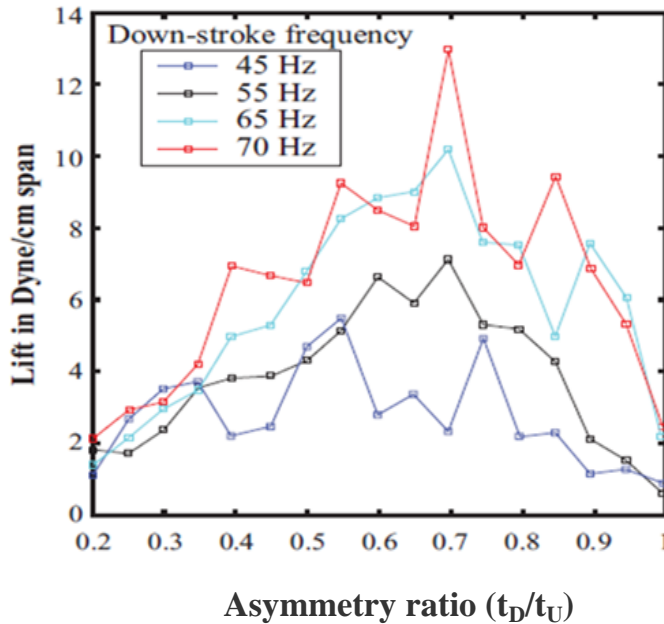


Figure 1.5: Result of 2D discrete vortex simulations. 45 rev/s corresponds to $Re \sim 1200$ (Other values of Re increase linearly with increase in frequency of flapping). Amplitude of flapping = 80° , mean position of wing = -20° , wing length = 1 cm (Devranjan, 2009)

The aim of the present work is to verify these findings for a 3-D wing case, using quantitative flow visualization techniques (PIV). Furthermore, this work is used as a benchmark for 3D lattice Boltzmann simulations done in our group (Kritivasan, 2016).

This thesis is structured as follows. The second chapter describes the experimental setup. The third and the fourth chapter, present the qualitative and quantitative results respectively. Chapter five concludes the work done and outlines future experiments. Some of the additional details on the experiments and analysis are presented in the appendices.

CHAPTER 2

EXPERIMENTS

We wish to study the effect of asymmetry in flapping, on the flow field. To this end, our approach has been to measure the velocity field for the fluid surrounding the wings. The experiments, thus, have been designed taking that in consideration.

This chapter first discusses the various components of the experimental set-up, which is followed by an overview of the flapping motion prescribed to the body. Subsequently, the details of the experimental technique used to explore the flow field are presented. Finally, the various parameters in the experiments and the non-dimensional numbers are described.

This chapter deals with another important issue with regard to experiments. How does one establish a protocol for experiments, where there is no instantaneous repeatability?

2.1 Experimental Setup

Experiments are carried out in a glass tank (1m X 1m X 0.8m) with water. A Flapper Mechanism was designed and mounted vertically inside this glass tank to conduct PIV experiments. Some salient features of this design are:

- Drive Assembly: A pulley- gear assembly was designed to provide necessary one-to-one rotation of opposite hand using only one motor.

| Spur gears (Plastic) | Timing Pulley |
|-----------------------------|----------------------|
| Pitch dia: 37.5mm | Pitch dia: 12.8mm |
| Module: 1.5 | Pitch: 2.5mm |

- Coaxial Shafts (Stainless Steel) to achieve counter rotation of the wings

| Inner Shaft | Outer Shaft |
|-----------------------------------|--|
| Solid Stainless Steel Dia: 6mm | Hollow Stainless Steel Outer Dia: 12mm, Inner Dia: 10mm |

- Wings: A pair of rigid, transparent, rectangular acrylic wings (thickness 3mm), where each wing is attached to a shaft. Therefore they have same rotational speed, but have opposite direction of rotation, giving rise to a flapping motion.
- Servo Motor²: To provide varying speeds, a servo motor is used.

A schematic of the mechanism is shown in figure 2.1 along with a photo of the counter-rotating drive mechanism

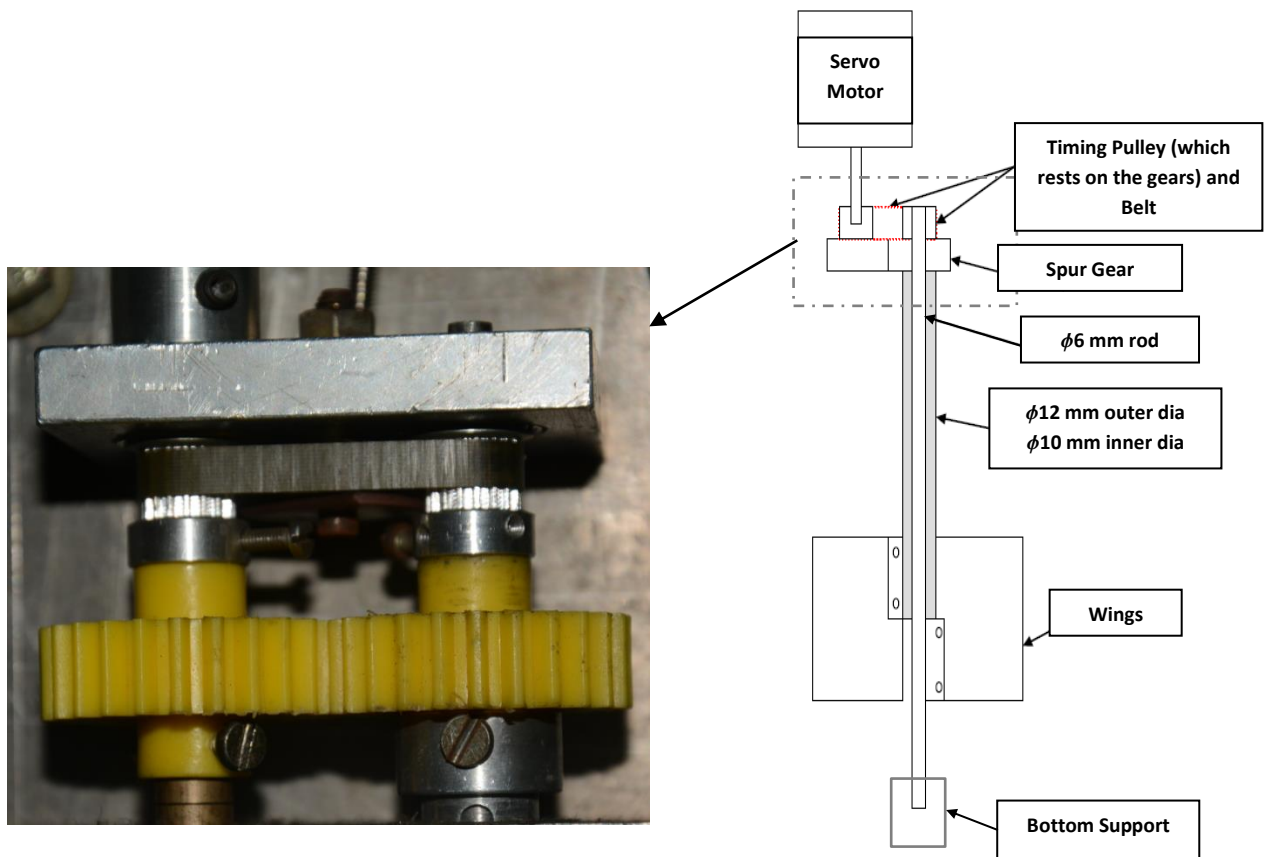


Figure 2.1: Schematic of flapping mechanism as well as photo of the drive assembly with timing pulley and spur gears.

This mechanism mounted vertically in the glass tank is held stationary with supports mounted on the sides as shown in figure 2.2 (a photograph of the experimental setup is shown in figure 2.3). To prevent any vibration because of the free end, the model is fixed to the bottom of the

² In the beginning, a stepper motor and a Galil motion controller were used for providing the flapping motion. But, using the stepper motor caused visible vibrations in the movement of the flapper. Therefore, a servo motor and drive were used instead.

tank. Furthermore, we take images from the bottom of the tank (using a mirror inclined at 45°) and not from the top (which is a free-surface), so that the surface waves do not distort the images when the wings are in motion.

As a result of the bottom support, a part of the inner radius region of either wing is not visible (this can be seen later in figure 2.9, when image of both the wings is taken). The portion of the flow that is not visible because of this, though, should have very low velocities and not have significant effect on the analysis done.

The Perspex flapping wings are attached to the mechanism using nuts and bolts. This small ($\sim 2\text{-}3\text{ mm}$) protuberance from the wing is assumed to cause negligible effect on the flow as the flow velocities close to the shaft are very small and the corresponding Reynolds number associated with this is ~ 5 . After mounting the mechanism in the glass tank, the assembly was checked for straightness as well (Appendix 1).

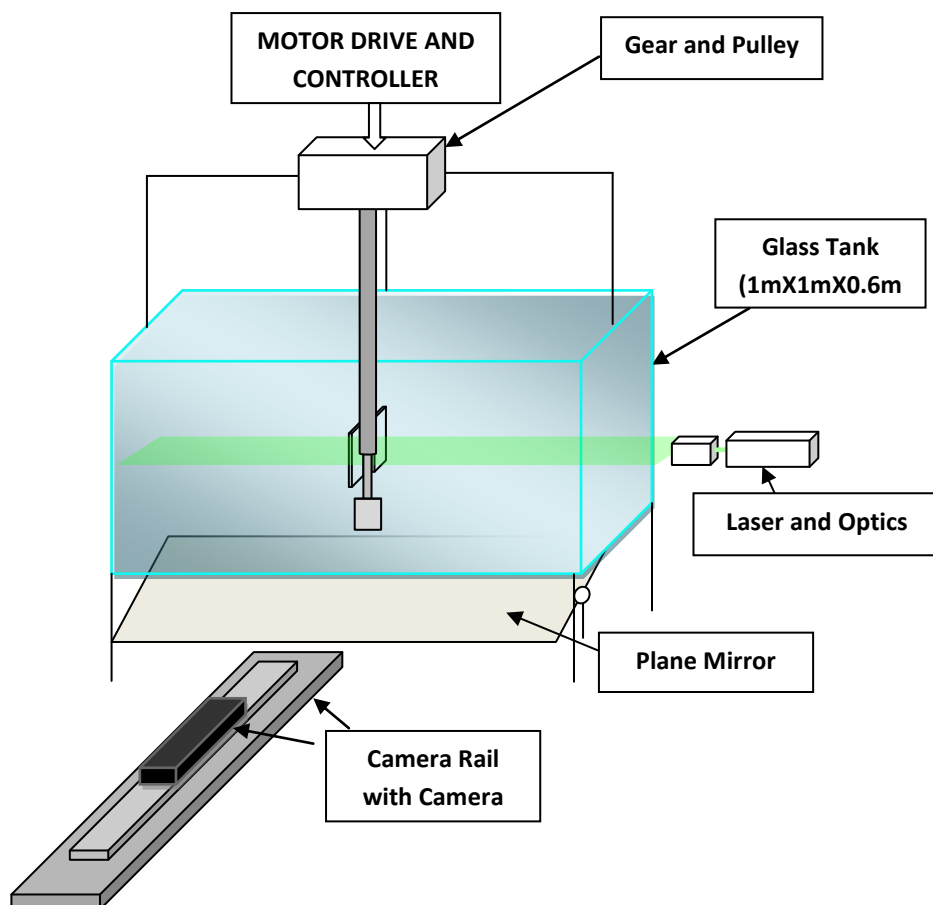


Figure 2.2: Schematic of Experimental Setup

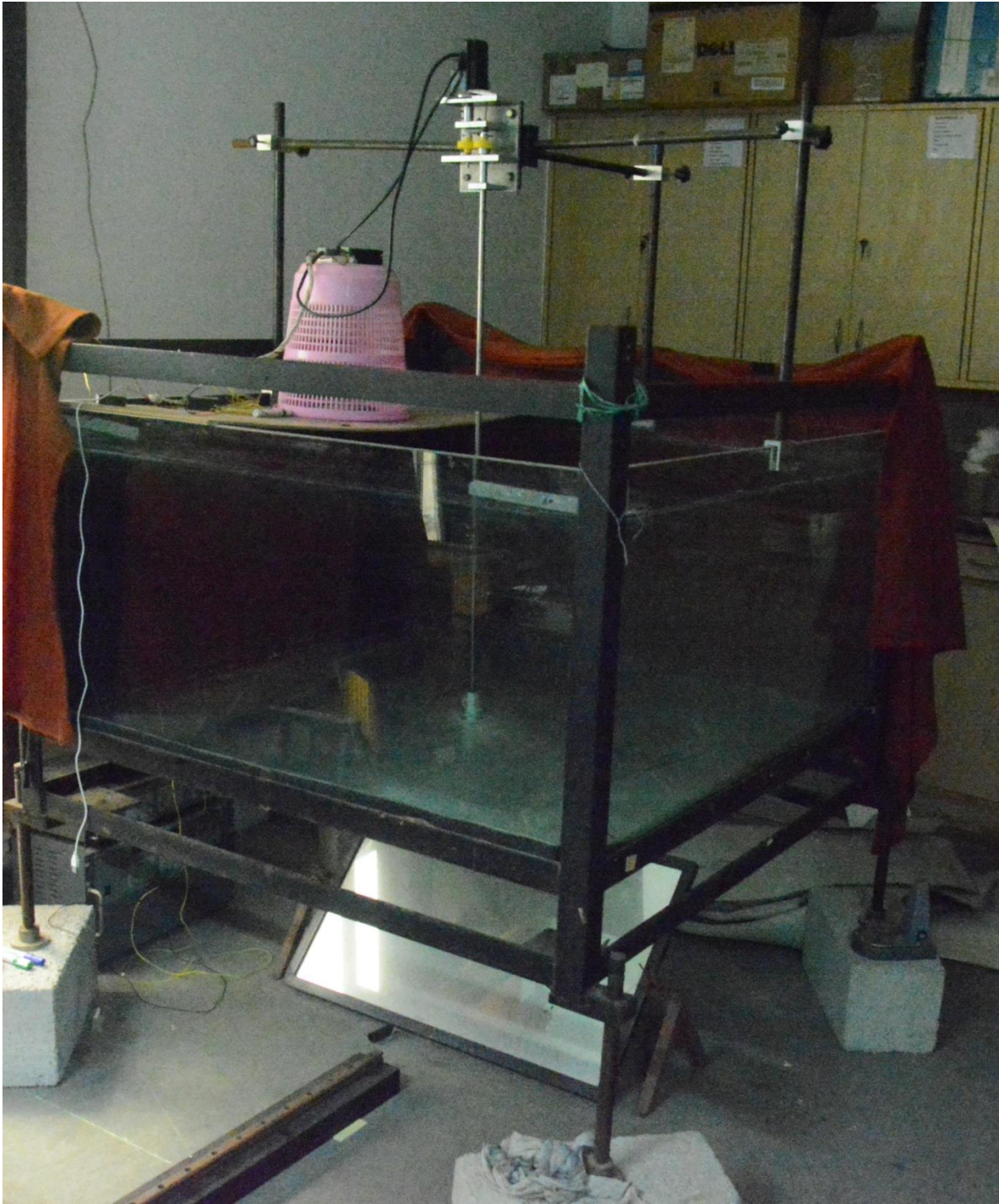


Figure 2.3: Photograph of Experimental Setup

2.2 Flapping Motion

The 2D discrete vortex simulations and flow visualization experiments done previously used a sinusoidal velocity profile of wing motion. But, the controller used in this case, did not provide for a direct way to give a sine-profile to the motor. Hence, a trapezoidal velocity profile with the smallest possible acceleration time was used instead, to minimize the effects of wing acceleration on the flow. The theoretical velocity profile (AR 1 to AR 0.6) given to the servo motor is shown in figure 2.4

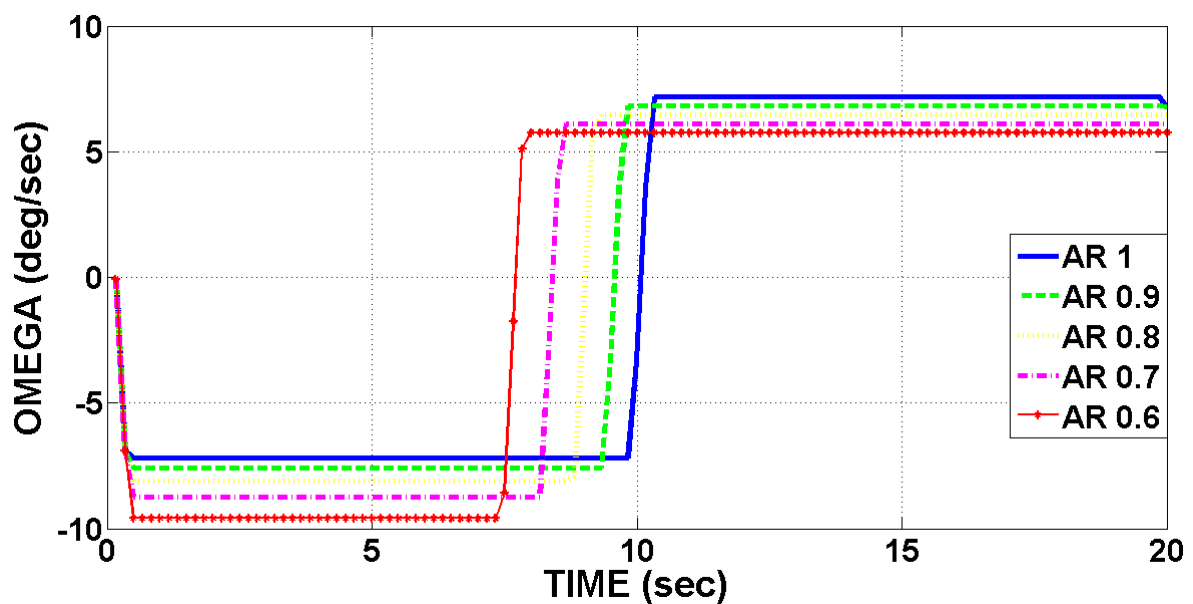
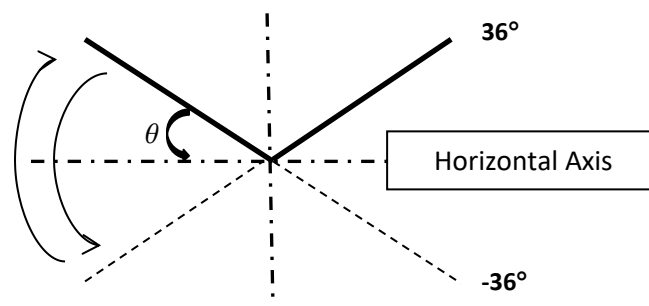
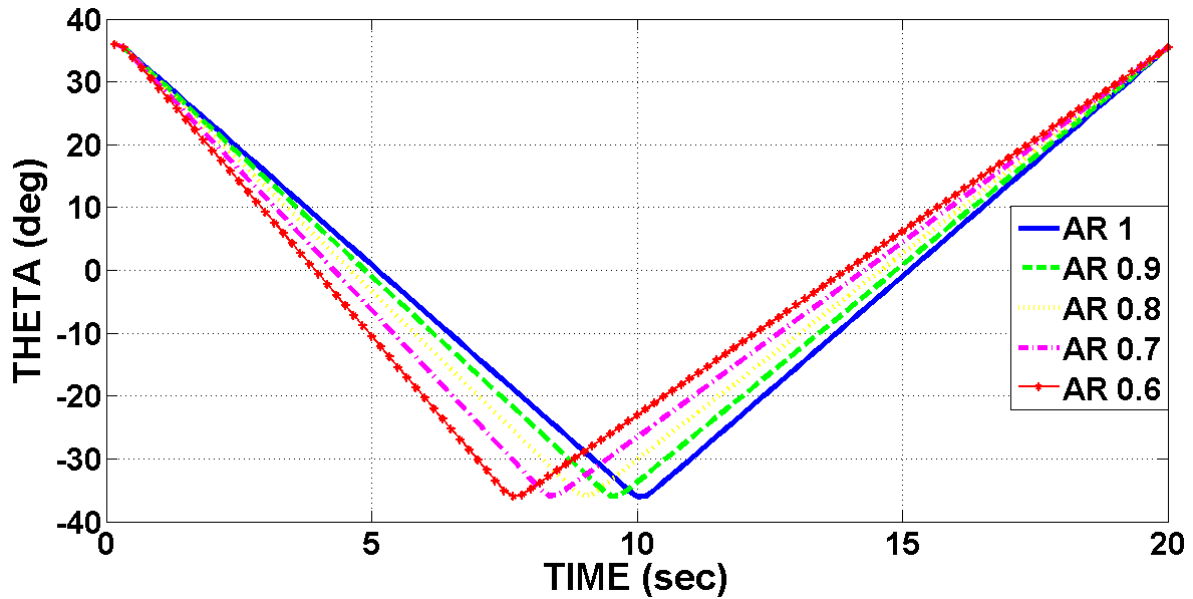


Figure 2.4: Theoretical velocity profile over a cycle or the velocity profile programmed into controller, for different asymmetry ratios

The corresponding angular position profile can be seen in figure 2.5 (b)



(a) schematic showing flapping motion of wing



(b)

Figure 2.5: (a) shows a Schematic to give an idea of how theta is measured with respect to the wing. (b) Presents the theoretical theta (angular position) profile over a cycle, as a result of the programmed velocity profile, for different asymmetry ratios

2.2.1 Tracking the wing motion:

The laser sheet when incident on the wing causes a reflection which is visible in the PIV images taken. This reflection is used to track the wing position using a custom automated tracking algorithm written in MATLAB. We first threshold the image, then perform morphological operations to separate the wing-laser intersection from the seeding particles. After this, we use Hough Transform (Appendix 2) to get the angular position of the wing with respect to the bottom edge of the image.

Figure 2.6 shows the angular position that has been extracted for different AR's from 200 images captured in one cycle. It can be seen that the actual wing motion is consistent with the input profile, figure 2.5(b). The fluctuations in the graph, especially the high intensity ones, are because of the error in extracting one representative line from the area of brightly lit pixels that is the reflection of the wing. The low amplitude fluctuations (that are present in all curves, consistently throughout the cycle) though, could also be because of small amplitude vibrations present in the wing motion.

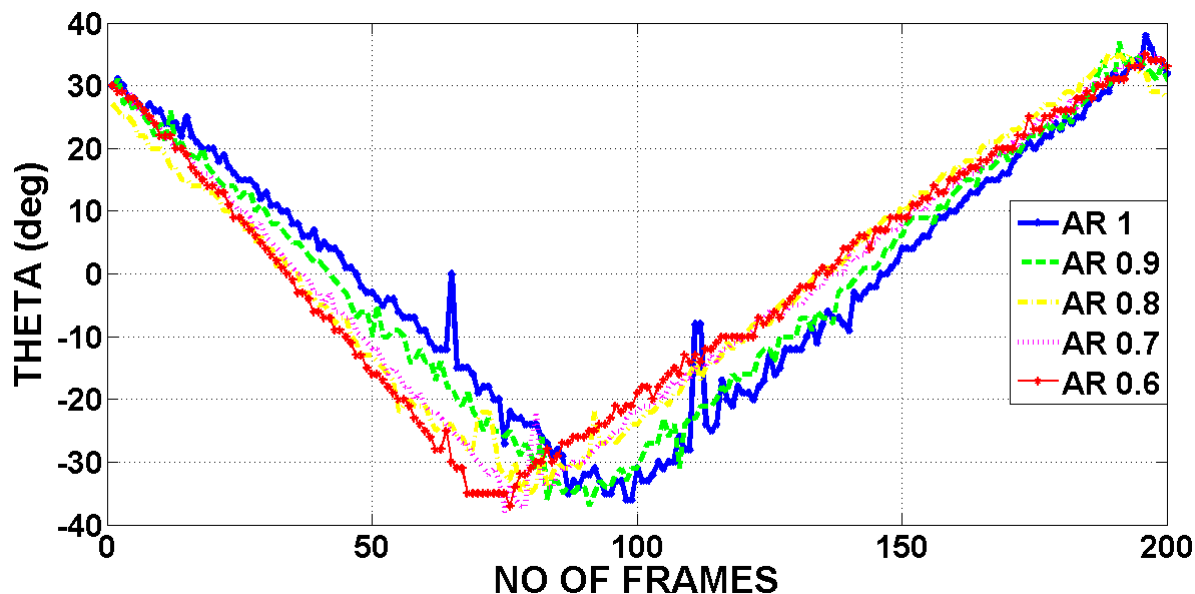


Figure 2.6: Example of actual theta profile over a cycle extracted from experimental images, for different asymmetry ratios: 200 frames per cycle, Image recording frequency.

Controller:

- Arcus-ACE-SXE. Allows an S-curve feature (smoothing of profile), although not used in current experiments)
- For the first 2 sets of experiments presented here a different controller was used: Arcus PMX 4 axis stepper motor controller, although it worked just as well for the servo motor.
- Motor has been programmed using software available on the company website

Motor: JMC 200 W servo motor, model no: 60ASM200

| Item | 60ASM200 |
|----------------------------|----------|
| Supply voltage (V) | 36 |
| Rated power (W) | 200 |
| Rated torque (N.m) | 0.637 |
| Peak torque (N.m) | 1.91 |
| Rated speed (rpm) | 3000 |
| Rated armature current (A) | 7.6 |
| Moment coefficient (N.M/A) | 0.0918 |

| Item | 60ASM200 |
|----------------------------|----------|
| Motor frame size (mm) | 60 |
| Motor flange diameter (mm) | 50 |
| Motor shaft diameter (mm) | 14 |
| Shaft length(mm) | 27.5 |
| Motor length(mm) | 134 |

In the assembled system, it was observed, that there is a stoppage time (~ 100 ms) when there is a change in the direction of the motor (down-stroke to up-stroke or vice-versa). This is probably due to that high starting torque required while changing direction (delay because of controller programming is only ~ 10 ms). To avoid this, especially at higher flapping speeds, a gear-reducer can be used in future experiments, so that the motor gives higher torque at low speeds.

2.2.2 Repeatability of Wing Motion

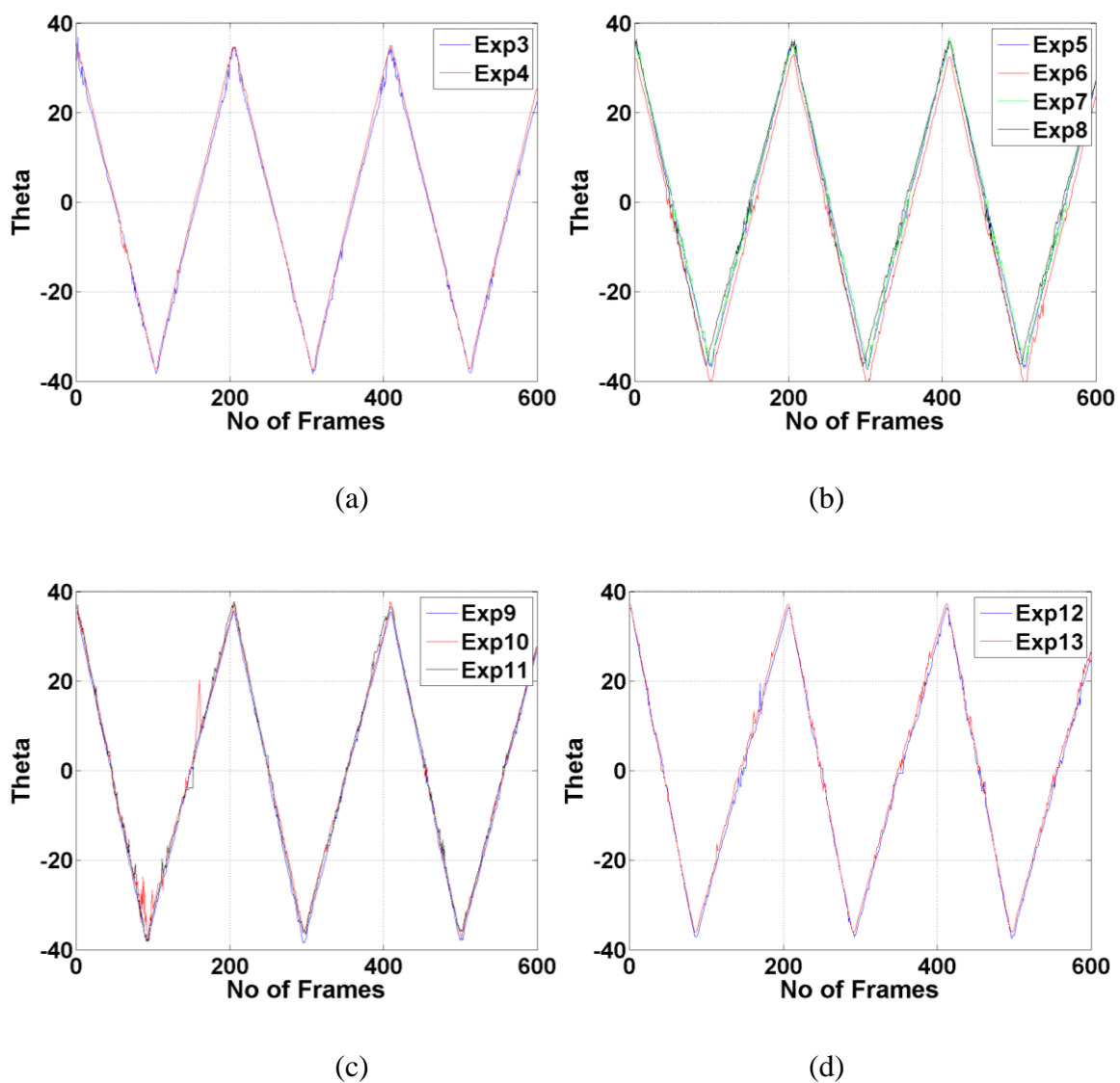


Figure 2.7: Actual theta profile over a cycle extracted from experimental images (200 frames per cycle) for different sets of experiments, $Re = 314$, (a) $AR = 1$, (b) $AR = 0.9$, (c) $AR = 0.8$, (d) $AR = 0.7$

Figure 2.7 compares the actual wing motion (extracted as explained in the previous section) for multiple runs done.

- Wing Motion is similar to up to 2-3°
- In the figure (c), the jump in the first cycle of Exp 10 is because of the limitations of the theta extraction method. The actual wing motion is smooth in all cases.

2.3 Particle Image Velocimetry

Particle Image Velocimetry (PIV) is a quantitative flow visualization technique, using which the velocity vector field for the region of interest can be obtained.

The working medium (water in our case) is seeded with tracer particles, sufficiently small so that they follow the local flow.

- Velocity lag (to a fluid acceleration \mathbf{a}) = $d_p^2 \frac{(\rho_p - \rho)}{18\mu} \mathbf{a} \sim (10^{-5} \mathbf{a})$ m/s, for our case

(Raffel, Willert, & Kompenhans, 1998)

d_p : Particle size (50 μm)

ρ_p : Density of Particle (1030 kg/m^3)

ρ : Density of water (1000 kg/m^3)

μ : Dynamic viscosity of water $\sim 10^{-3}$ N.s/ m^2

Since accelerations in this system aren't very high (~ 0.02 m/s^2) this is very small in comparison with the velocity scale in our system (average tip speed $\sim 10^{-3}$ m/s)

- Relaxation time = $d_p^2 \frac{\rho_p}{18\mu} \sim 10^{-3}$ s (Raffel, Willert, & Kompenhans, 1998)

These are then illuminated with a laser sheet (Litron Nd:YAG pulsed laser, 100 mJ/pulse, used at 10 Hz), and the scattered light is recorded using a high speed camera (IDT Motion Pro-Y5, in our case). Successive images are used to calculate the displacement of a group of particles in a given time using cross-correlation. This calculation gives us the velocity vector field of the entire illuminated flow at each time instant.

Adaptive correlation is used in *Dynamic Studio* (Dantec) for calculation of PIV vectors. Interrogation window size was generally taken to be 32X32 pixel² with 50% overlap, and validation using moving average.

Further post-processing of vectors (calculation of derivatives, lift etc.) is done later using Matlab®. The gradients of vectors are calculated using the least squares method. While plotting vector and vorticity, the vectors have been normalized with the average tip velocity of the wing and vorticity has been normalized with the flapping frequency ($1/\text{Time-period}$).

Since we conduct the experiments in water (ν almost ten times less than air), it allows us to run the model at low speeds, and helps in better flow visualization. Additional details of PIV pertaining to all experiments done have been given in section 2.4. It should be noted that in the experiments done, the flapping wings, the camera and the laser were triggered together using a transistor-switch. This allowed us to compare across experiments much more easily, because they started at the same time.

Figure 2.8 shows a comparison between streaks (obtained by overlapping successive PIV images) and corresponding velocity vectors.

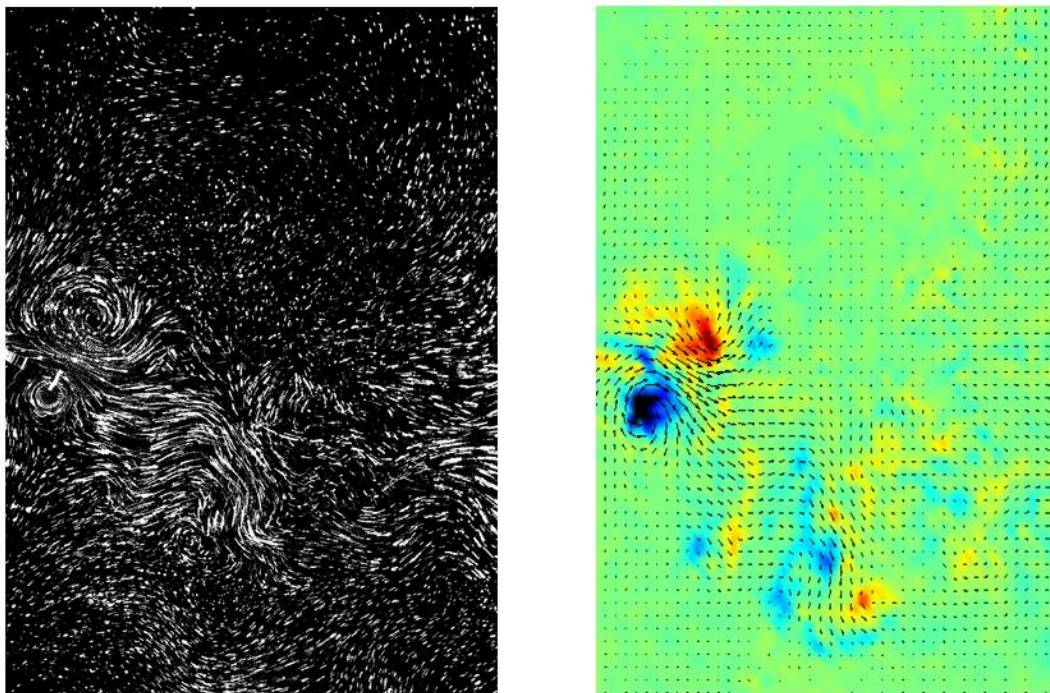
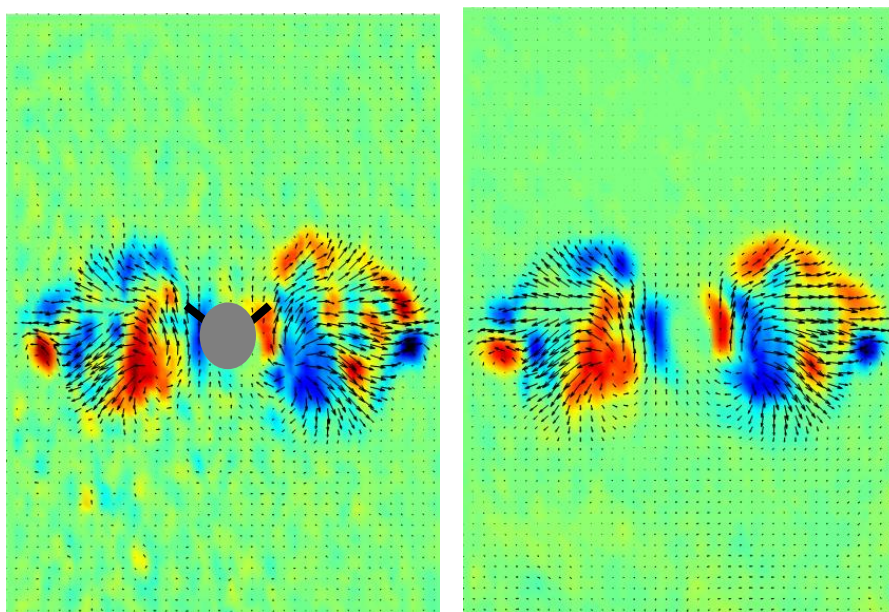


Figure 2.8: Example of instantaneous streaks and corresponding velocity and vorticity fields for $Re = 628$, $AR = 0.6$. The colour represents vorticity, and the axis has been suitably chosen to show comparison with streaks

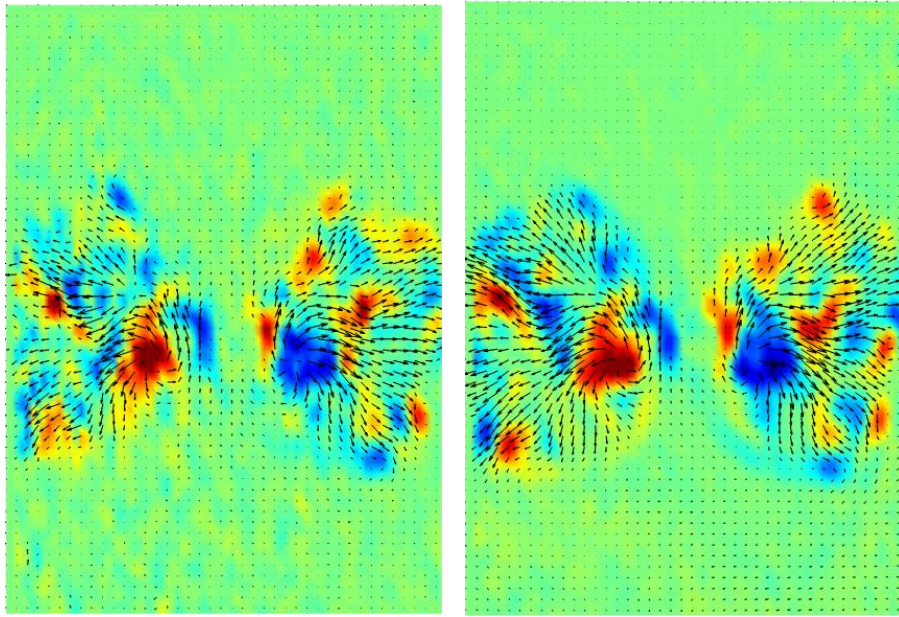
2.3.1 Repeatability of PIV

Since there can be no surety that the flow reaches a periodically steady state, even though the wing motion is periodic, it is not straight-forward to define repeatability for this flow. All the experiments conducted were started from a state where there is little or no motion of the ambient fluid. But the flow-field doesn't match instant-to-instant for experiments with the same set of parameters.

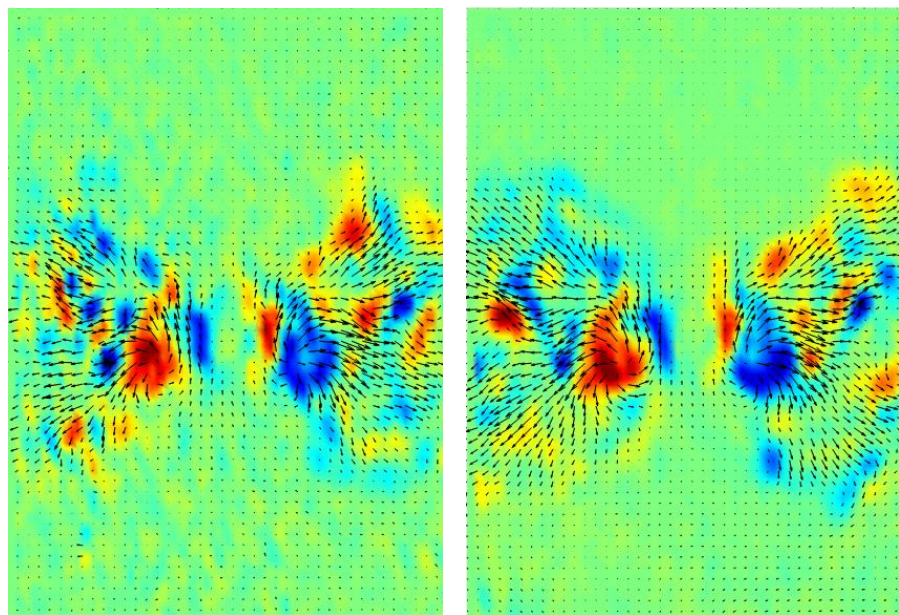
Figure 2.9 (a) to (d) shows that the general structure and extent of the wake looks similar



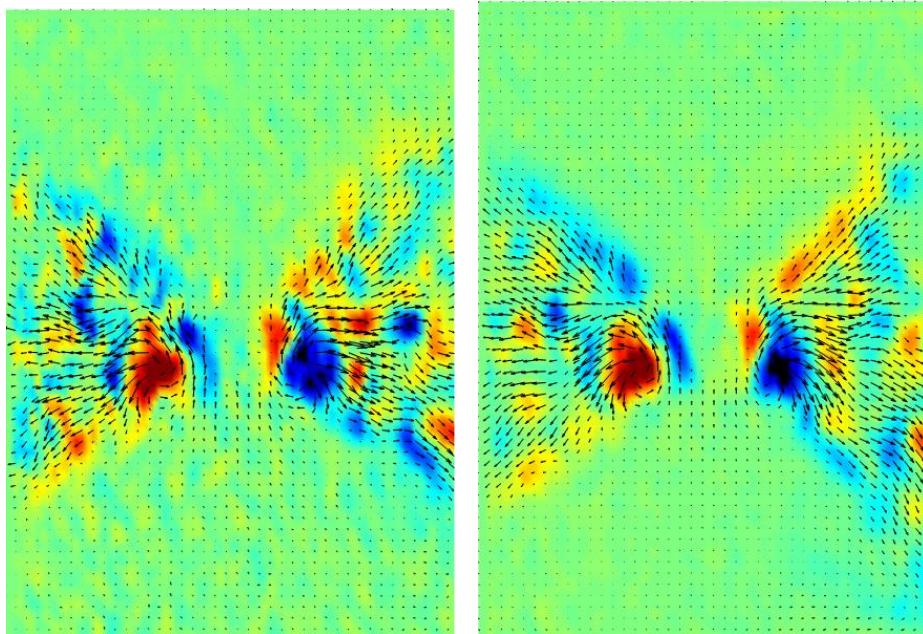
(a) End of 2nd Cycle (with position of wing and bottom support)



(b) End of 3rd Cycle



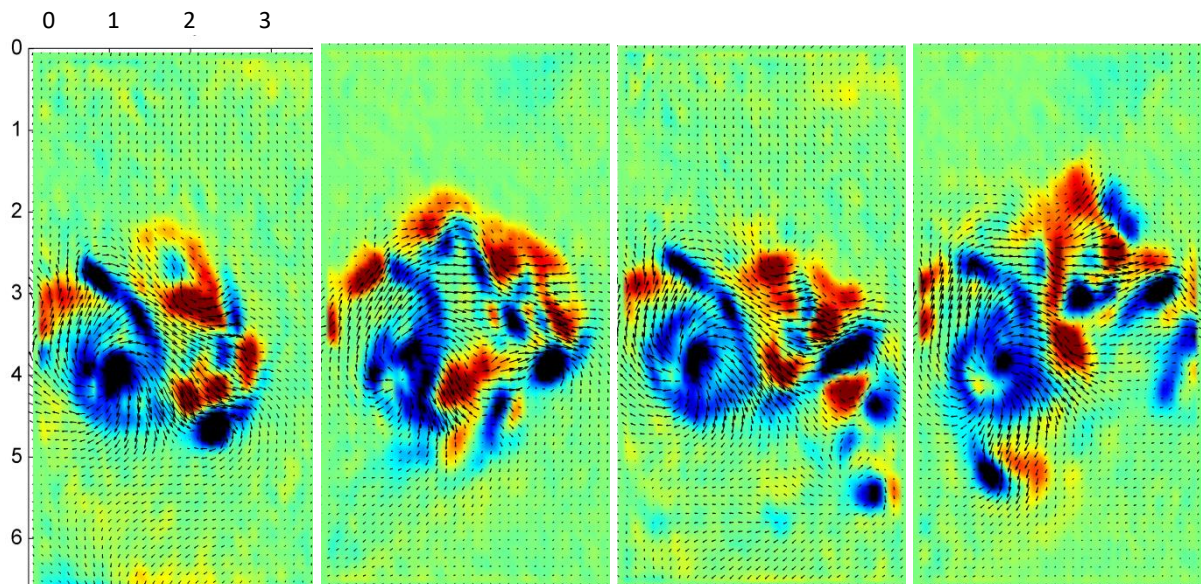
(c) End of 4th Cycle



(d) End of 10th Cycle

Figure 2.9: Velocity and vorticity fields for 2 different experiments (two-wings) $Re = 314$, $AR = 1$, at the end of different cycles (a)-(d).

But, looking closely, detailed flow direction and structures are very different at the corresponding instant, as shown in figure 2.10



(a) End of 2nd Cycle

(b) End of 3rd Cycle

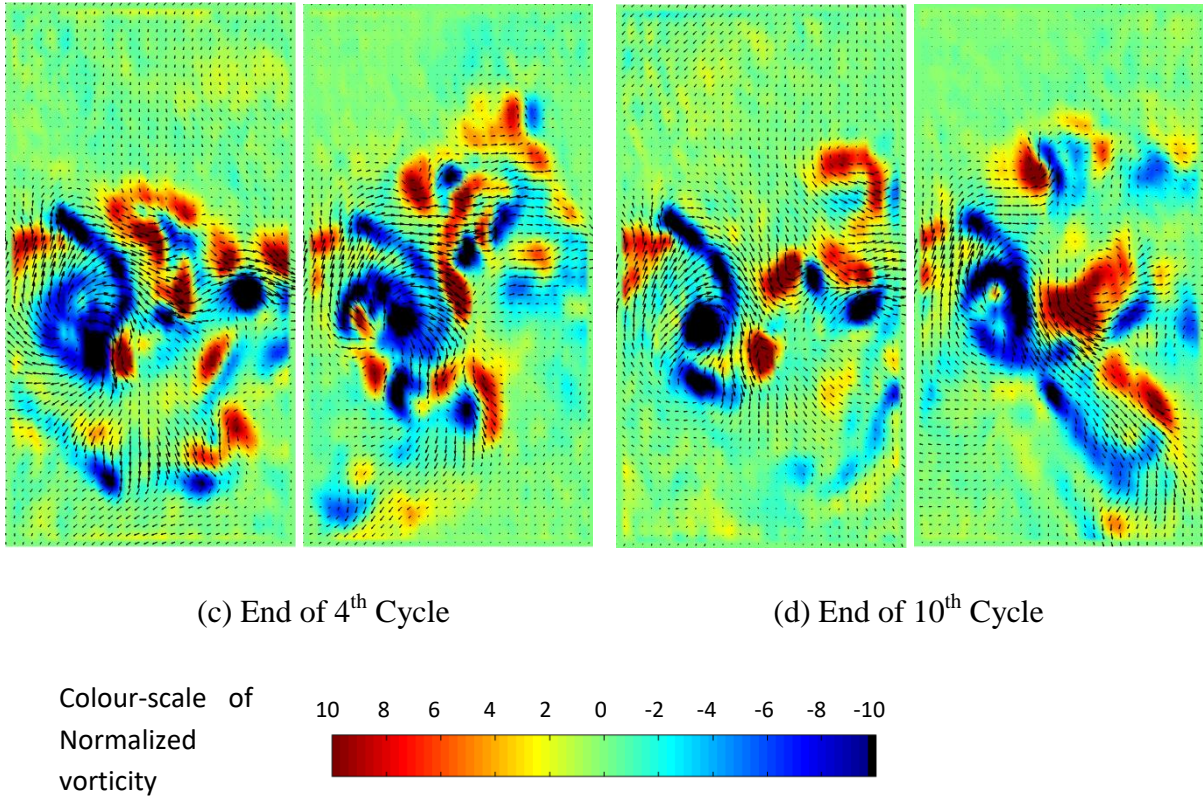


Figure 2.10: Velocity and vorticity fields for 2 different experiments (one-wing) $Re = 314$, $AR = 1$, at end of different cycles (a)-(d). Horizontal scale: 0 - 3.5, Vertical scale: 0 - 6.5 (normalized with the span of one wing). Vorticity values have been normalized with the Time-Period of flapping; the colour bar is as show. All the velocity-vorticity plots shown henceforth, therefore, have the same horizontal-vertical extent and the same vorticity scale.

This may be because of the “little or no motion” of the ambient fluid before the start of each experiment. The ambient never went to a state of complete rest. This is even after waiting up to 1-2 days for any motion to settle down! Because of this, we had trouble defining any set protocol for our set of experiments (The setup can be closed and isolated from the atmosphere to avoid any velocity induced because of air currents. For example, a glass box can be used instead of a glass tank for the experiments).

But, these differences do average out, to an extent, over large times (~ 20 flapping cycles in this case). In other words, by seeing the similarity in forces (calculated from the velocity-field) for experiments, we can say that on average, the flow is similar when the wing motion is the same.

Finally, all the experiments presented here have been performed after waiting for the flow to settle down sufficiently. This generally meant that there is a gap of at least 3-4 hours between experiments.

2.4 Experimental conditions and Non-Dimensional Numbers:

Key non-dimensional parameters in the experiment are Re and AR:

- $Re = 2Afs^2/\nu$ (based on average tip-speed of wing: $2Afs$)
($f = 1/T$)
($A =$ amplitude of flapping, 72°)
($s =$ span of one wing, 5 cm)
($\nu =$ kinematic viscosity of water $\sim 10^{-6} \text{ m}^2/\text{s}$)
- Asymm Ratio (AR) = t_d / t_u
($t_d =$ down-stroke time)
($t_u =$ up-stroke time)
($T = t_u + t_d$, Total time-period)

Other important parameters that are not varied in this thesis

- Aspect Ratio = span/chord (1/3 for all sets of experiments)
- Amplitude of Flapping (total θ in during up-stroke or down-stroke, $A = 72^\circ$ for all experiments)
- The velocity profile considered here is trapezoidal with a high (with respect to the average angular velocity) acceleration $\sim 40^\circ/\text{sec}^2$

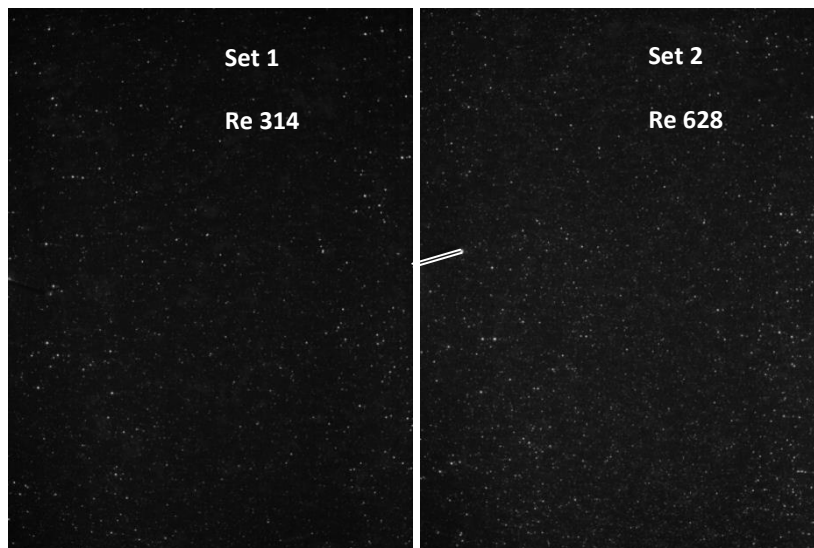
All the data presented in this thesis is from 5 sets of experiments done. In particular, all the velocity-vorticity plots presented henceforth are from set 4. The velocity and vorticity-field when presented follow the convention laid down in figure 2.10

| <i>Parameters</i> | Re 314 (2014/10/25) Set 1 | Re 628 (2014/10/25) Set 2 | Re 314 (2015/06/03) Set 3 | Re 314 (2015/06/07) Set 4 | Re 314 (2014/12/27) Set 5 |
|---|---|---|---|---|---|
| Θ | 72° | 72° | 72° | 72° | 72° |
| <i>Time period</i> | 20 s | 10 s | 20 s | 20 s | 20 s |
| Δt | 200 ms | 200 ms | 100 ms | 100 ms | 200 ms |
| <i>Wing (span X chord)</i> | 5 X 15 (cm) | 5 X 15 (cm) | 5 X 15 (cm) | 5 X 15 (cm) | 5 X 15 (cm) |
| <i>PIV Particles used</i> | 30 μ hollow glass spheres (0.6g/cm ³) | 30 μ hollow glass spheres (0.6g/cm ³) | Dantec Dynamics 50 μ PSP round particles (1.03g/cm ³) | Dantec Dynamics 50 μ PSP round particles (1.03g/cm ³) | Dantec Dynamics 100 μ PSP round particles (1.03g/cm ³) |
| <i>Thickness of Laser sheet</i> | Thinnest in the middle (1mm near wing), but thicker(up to 10mm) elsewhere | Thinnest in the middle (1mm near wing), but thicker(up to 10mm) elsewhere | Thin (1mm or less) throughout the observed area | Thin (1mm or less) throughout the observed area | Thinnest in the middle (1mm near wing), but thicker(up to 10mm) elsewhere |
| <i>Total area</i> | 425mmX314 mm (2336 X 1728 pixel ²) | 425mmX314 mm (2336 X 1728 pixel ²) | 303mmX184 mm (2256 X 1384 pixel ²) | 337mmX181 mm (2000 X 1072 pixel ²) | 457mmX338 mm (2336 X 1728 pixel ²) |
| <i>Total Vectors</i> | 143 X 105 | 145 X 107 | 140 X 85 | 124 X 66 | 145 X 107 |

| <i>AR</i> | <i>1</i> | <i>0.9</i> | <i>0.8</i> | <i>0.7</i> | <i>0.6</i> |
|---------------|------------|--------------|--------------|--------------|--------------|
| Re 314 | $t_d = 10$ | $t_d = 9.5$ | $t_d = 8.9$ | $t_d = 8.3$ | $t_d = 7.5$ |
| | $t_u = 10$ | $t_u = 10.5$ | $t_u = 11.1$ | $t_u = 11.7$ | $t_u = 12.5$ |
| Re 628 | $t_d = 5$ | $t_d = 4.75$ | $t_d = 4.45$ | $t_d = 4.15$ | $t_d = 3.75$ |
| | $t_u = 5$ | $t_u = 5.25$ | $t_u = 5.55$ | $t_u = 5.85$ | $t_u = 6.25$ |

2.5 Seeding Density:

For all experiments done it was made sure that there were at least, 4-6 particles within a 32X32 (pixel²) area. An example PIV image of each of the experiments done is shown in figure 2.11



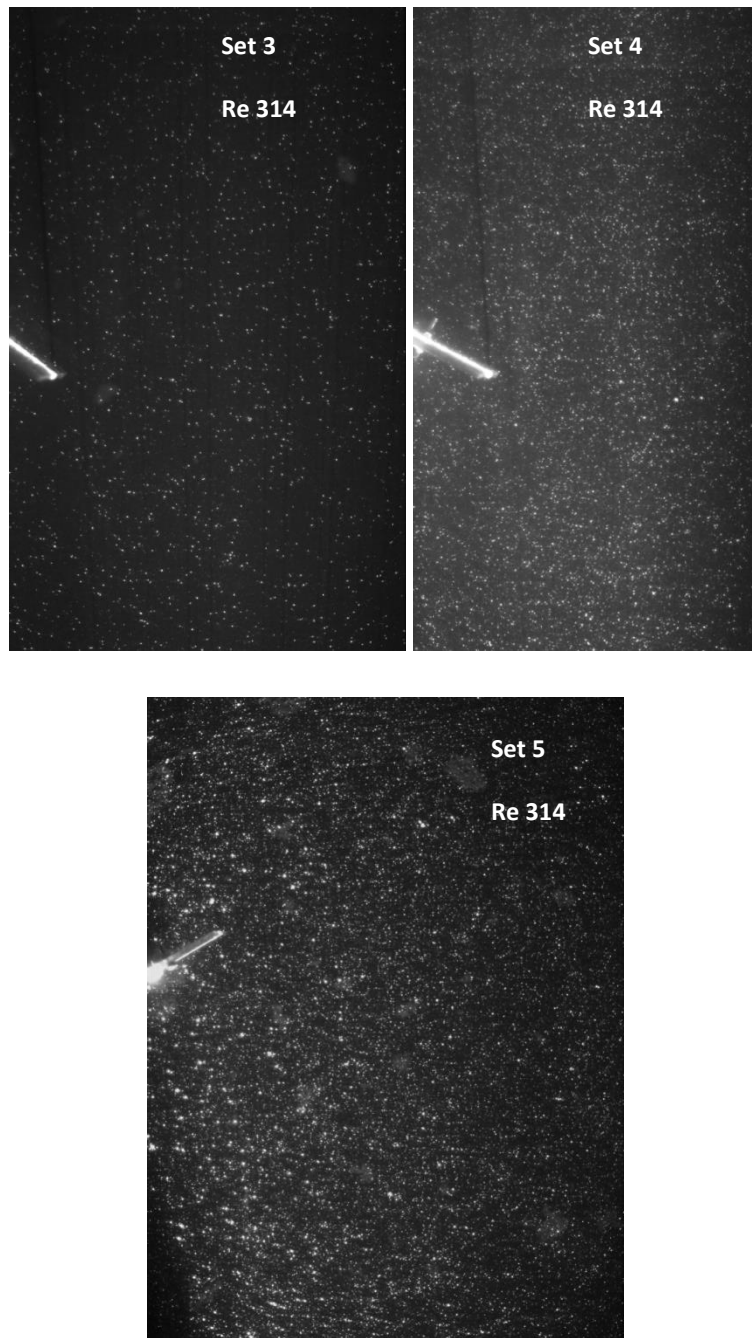


Figure 2.11: Example images showing seeding density for all the sets of experiments done

It should be noted that all one-wing, velocity-vorticity fields presented in this thesis henceforth are from set 4.

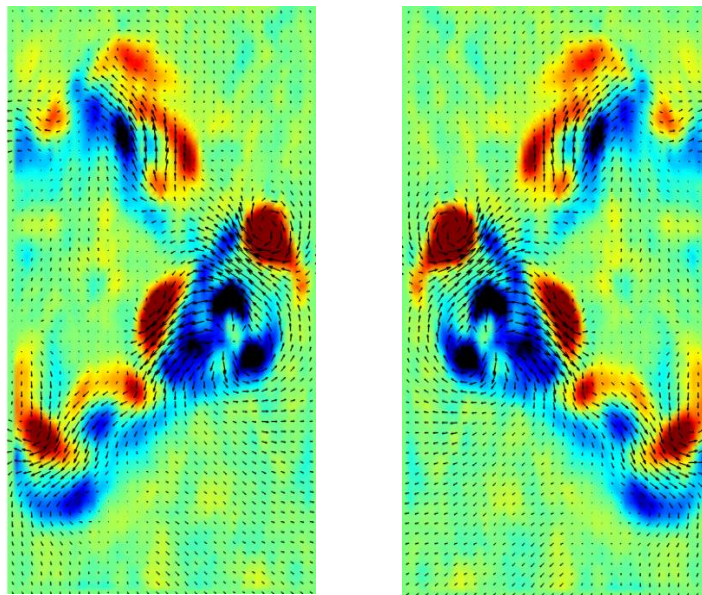
CHAPTER 3

RESULTS: QUALITATIVE OBSERVATIONS

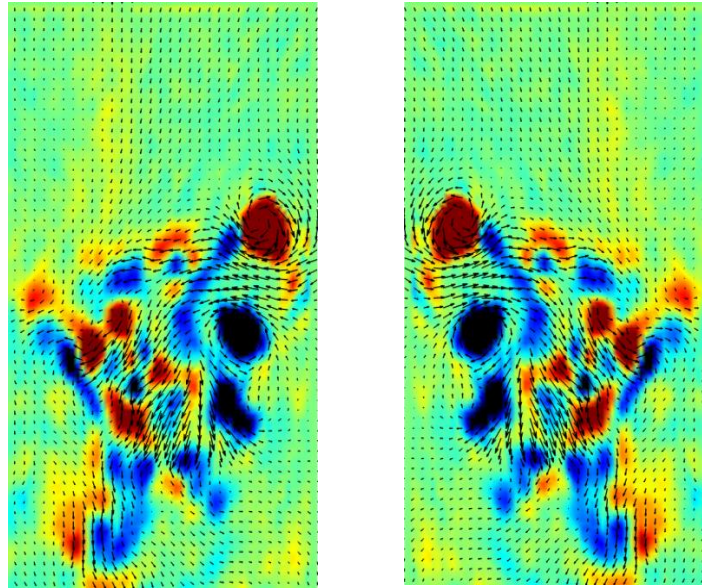
After obtaining the velocity field of the ambient fluid, the flow is best visualized using velocity-vorticity plots. Using such plots, the main features of the flow produced by the flapping wing are presented in this chapter.

3.1 “Two-Jet” or “Four-Jet”

The flow-field picture obtained here, shown in figure 3.1, from PIV experiments, reinforces the notion of “two-jet and four-jet” configurations, as observed previously by JV Shreyas (Shreyas, 2005)



(a) Symmetric flapping



(b) Asymmetric flapping

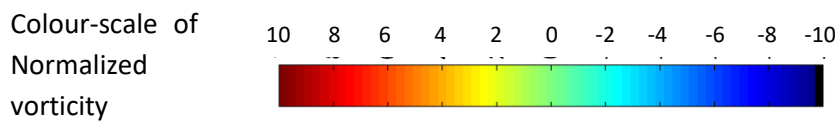


Figure 3.1: Instantaneous velocity and vorticity field $Re=314$, for (a) symmetric flapping ($AR = 1$), and (b) asymmetric flapping ($AR = 0.7$). Both plots, (a) and (b) have been obtained for the same wing. The left and right images in figure (a) and (b) are just mirror copies of each other and present the typical flow field.

While symmetric flapping pushes the fluid both above and below the wing, $AR = 0.7$, (or generally where the down-stroke is faster than up-stroke) has a net downward pushing effect on the surrounding fluid. This stronger downward jet in the case of asymmetric flapping would result in an upward force on the wing.

But the similarity with the flow picture obtained by Shreyas, is limited. There is no clear transition, from a “four-jet” to a “two-jet”, observed as we keep reducing the AR (going from symmetric to asymmetric), as was seen by them. What is observed instead, is that the downward jets keep getting stronger as AR is reduced.

It must be noted that the flapping wings used in experiments by Shreyas were almost 2D. Furthermore, Reynolds number for their experiment ~ 500 .

3.2 “Jet Meandering”

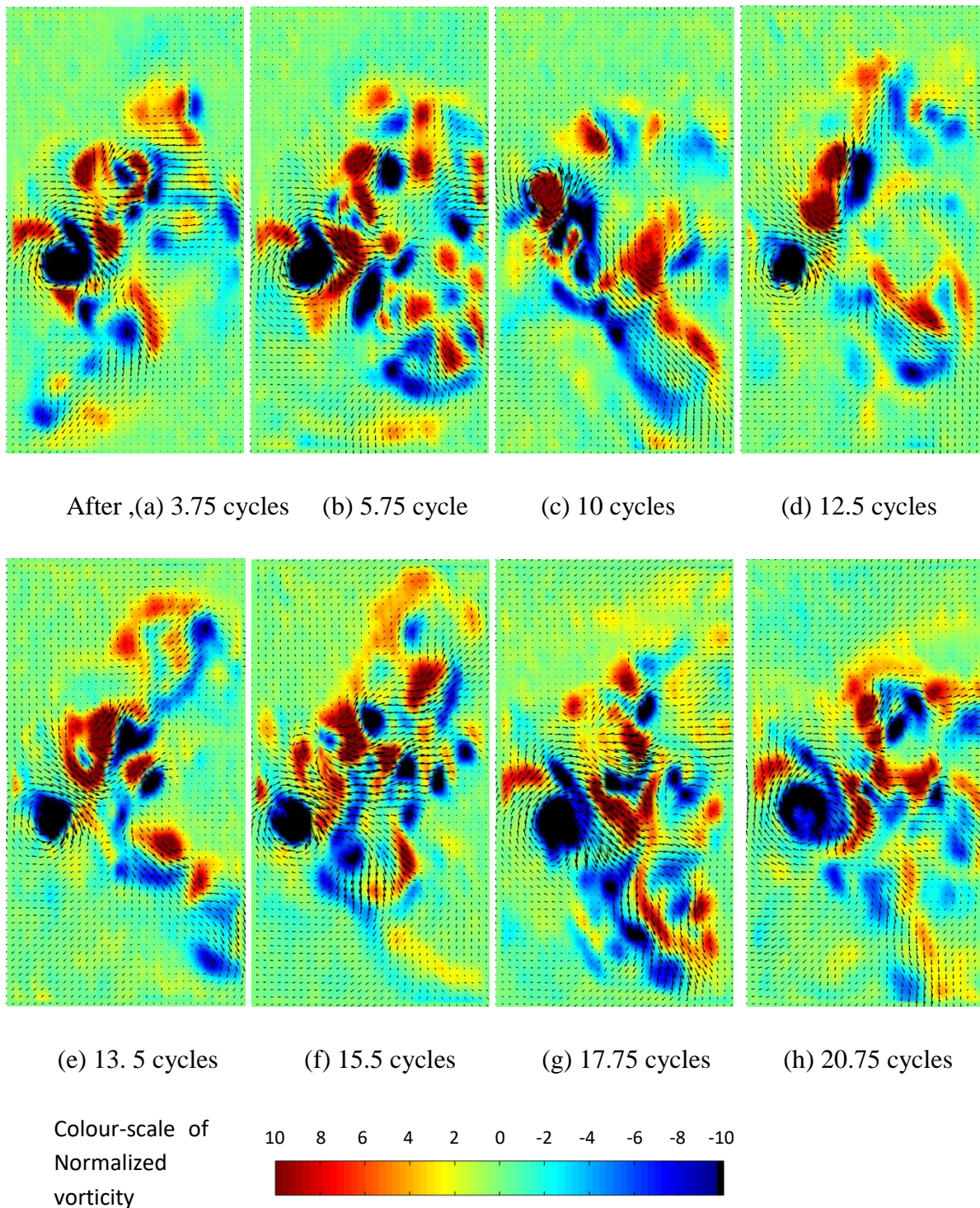
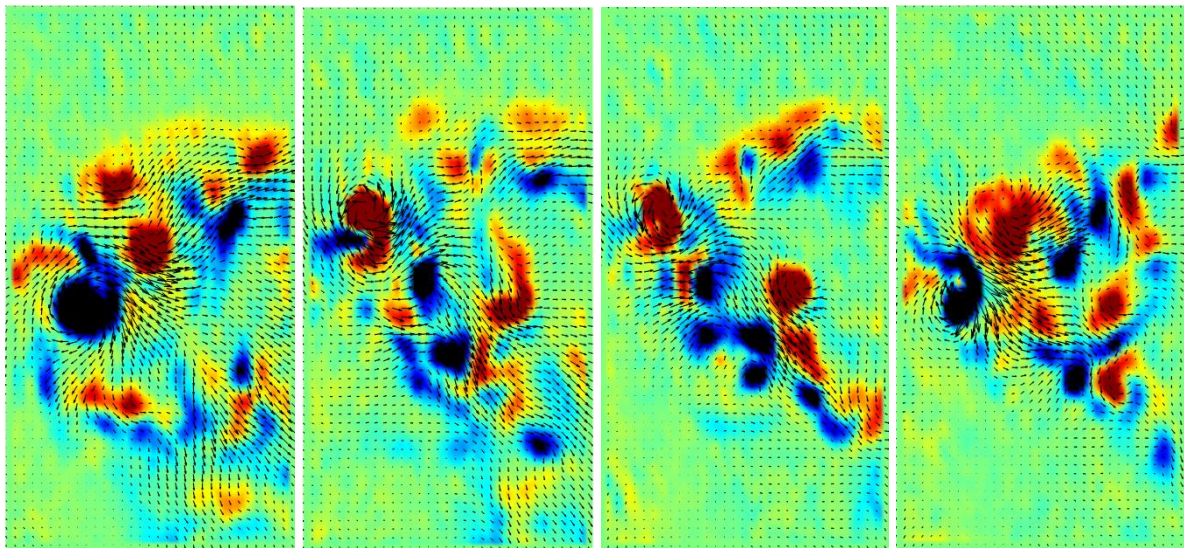
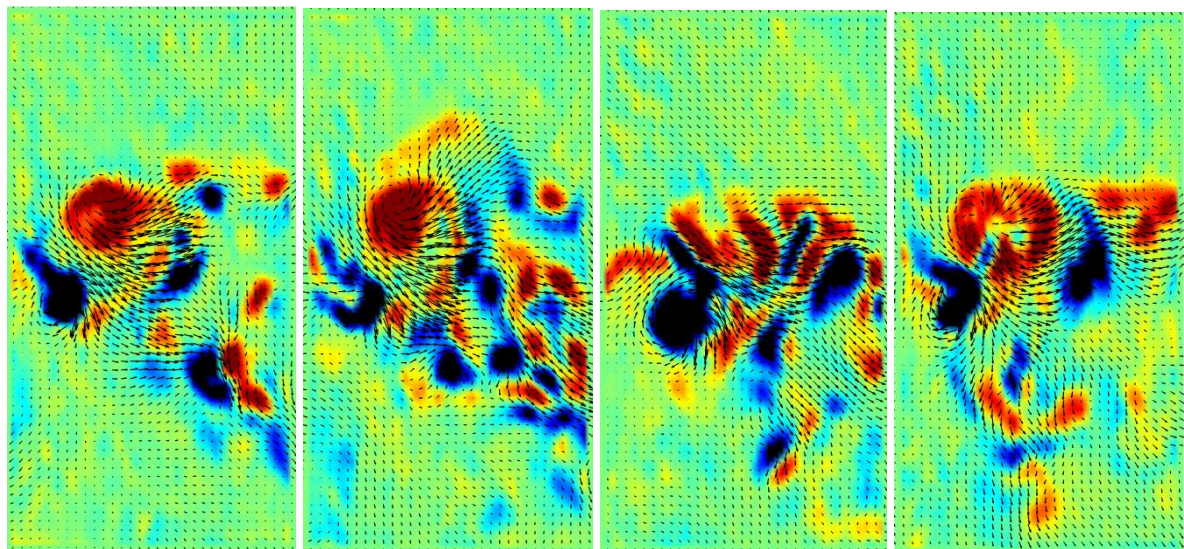


Figure 3.2: Instantaneous velocity and vorticity field $Re=314$, for symmetric flapping at different flapping-cycle times. See figure 2.10 for the corresponding vorticity scale.

Even though experiments have been done for up to 30 flapping cycles of the wing, it is seen that the flow doesn't reach a steady-state, or even a periodically steady-state. There is a continuous switching of the "jet" for all the AR's. In figure 3.2 (a)–(h), it can be seen that in symmetric flapping, jet position keeps switching from upward to 4-jet to downward.



After, (a) 3.75 cycles (b) 6 cycles (c) 9 cycles (d) 10.75 cycles



(e) 12.5 cycles (f) 14.5 cycles (g) 23.75 cycles (h) 29.75 cycles

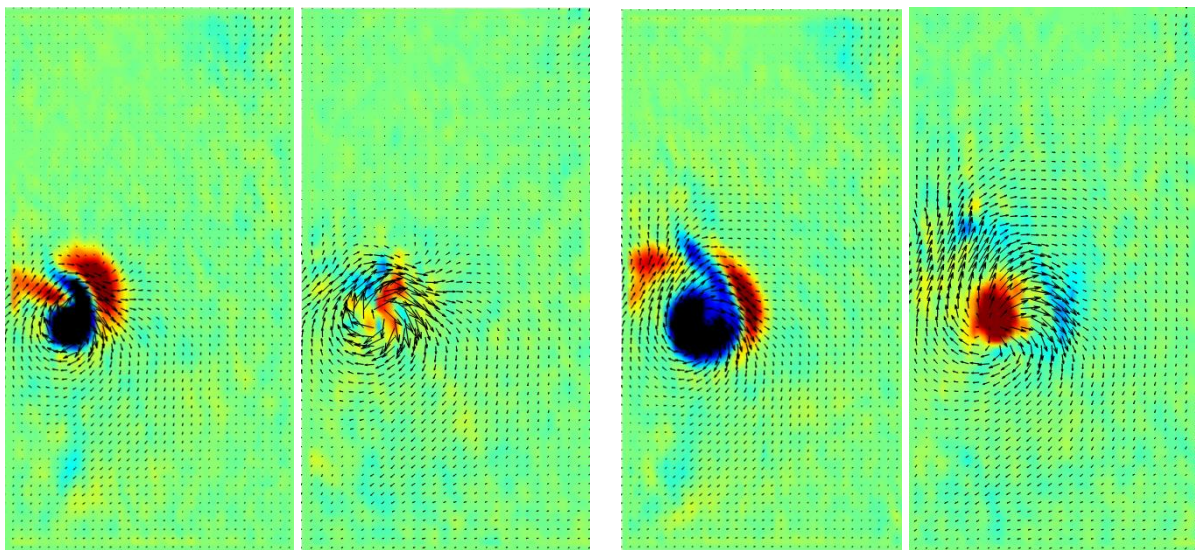
Figure 3.3: Instantaneous velocity and vorticity field $Re=314$, for asymmetric flapping ($AR = 0.7$) at different flapping-cycle times. Same vorticity scale as figure 3.2

Even for the asymmetric flapping case, shown in figure 3.3, over 30 flapping cycles from (a)–(h), a myriad of flow configurations can be seen, even though the net flow is downward. Jet position switches from a strongly downward, to a 4-jet, to a horizontal 2-jet. This “jet” switching behaviour has been previously reported for a 2-D rigid foil, flapping symmetrically (Shinde, 2012).

This switching of the jet is also seen as variation in control-volume force calculation (Refer to section 4.4).

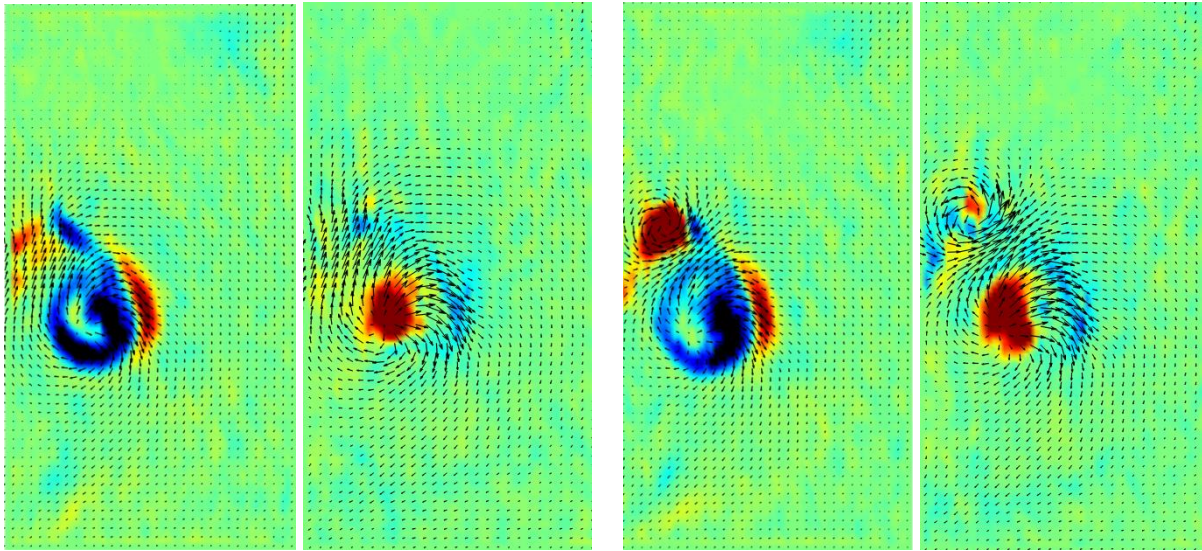
3.3 3-D Effects

In the flow-field picture obtained from PIV, it can be seen that the flow has a very strong 3D component. This causes a “splitting” of the vortex, that is being formed in the corresponding half-stroke. Dye visualization photos give an indication of this (appendix 3), but, this 3D effect is better visualized by plotting mass source value, $\frac{\partial u}{\partial x} + \frac{\partial v}{\partial y}$, for the flow. In a strictly 2D flow this term is zero (incompressible-flow, mass conservation). In this case, it therefore gives an idea of the “3D-ness” of the flow.



(a) Vorticity field and Source field

(b) Vorticity field and Source field

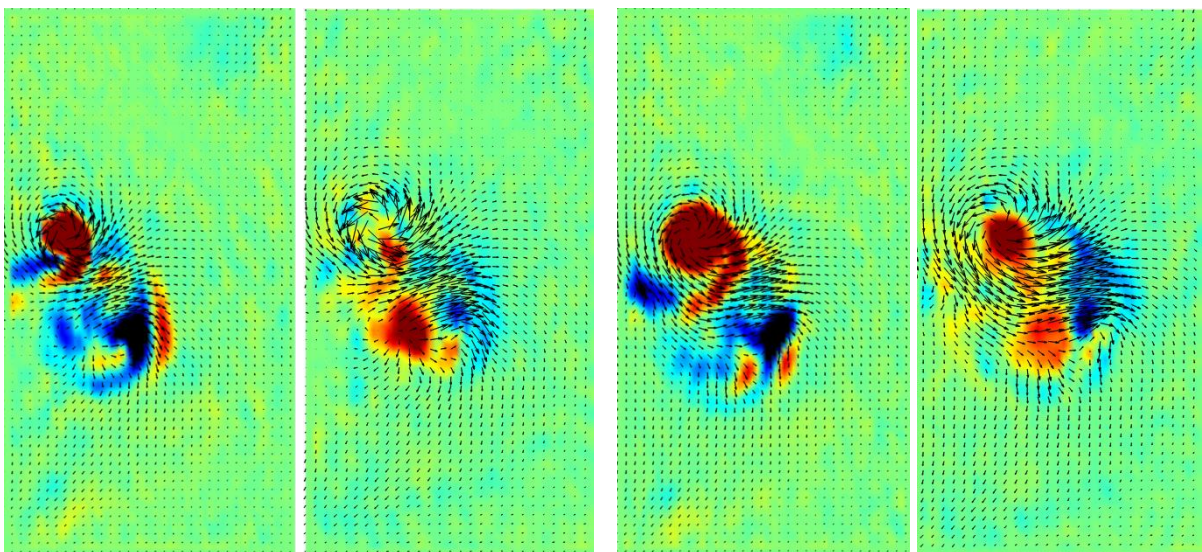


(c) Vorticity field and Source field

(d) Vorticity field and Source field

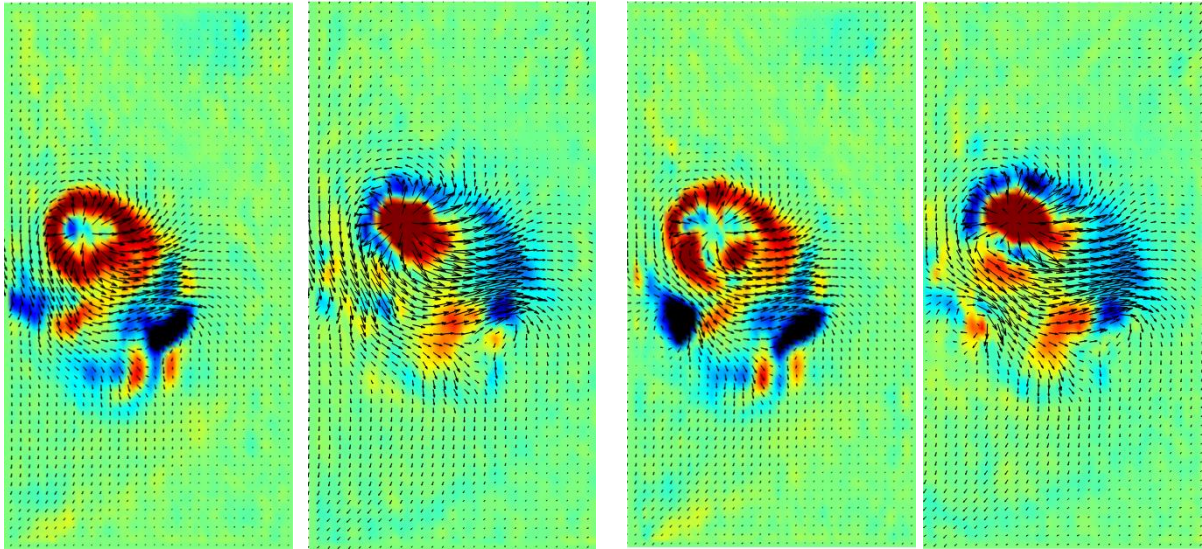
Figure 3.4: Comparison of instantaneous velocity-vorticity and velocity-source field, $Re=314$, for symmetric flapping during 1st flapping cycle ($t = 0.5T$ to $t = T$). The source term has also been normalized with the Time-Period of flapping and has the same scale as vorticity shown in figure 3.5

The panels in figure 3.4 and 3.5 show that the “source term” seems to be responsible for convecting vortices away from the wing (strong radially outward component).



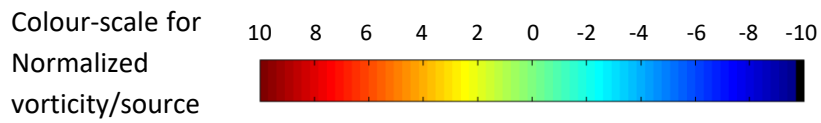
(a) Vorticity field and Source field

(b) Vorticity field and Source field



(c) Vorticity field and Source field (d) Vorticity field and Source field

Figure 3.5: Comparison of instantaneous velocity-vorticity and velocity-source field, $Re=314$, for symmetric flapping during 2nd flapping cycle ($t = T$ to $t = 1.5T$)



Furthermore, this source term is seen to accompany the production of each half-stroke (upstroke or downstroke) vorticity, except in the first half cycle as shown in figure 3.4 and 3.5 (a). On some thought, this source which is seen in the mid-plane of the wing, can be connected with the tip vortices as shown in figure 3.6

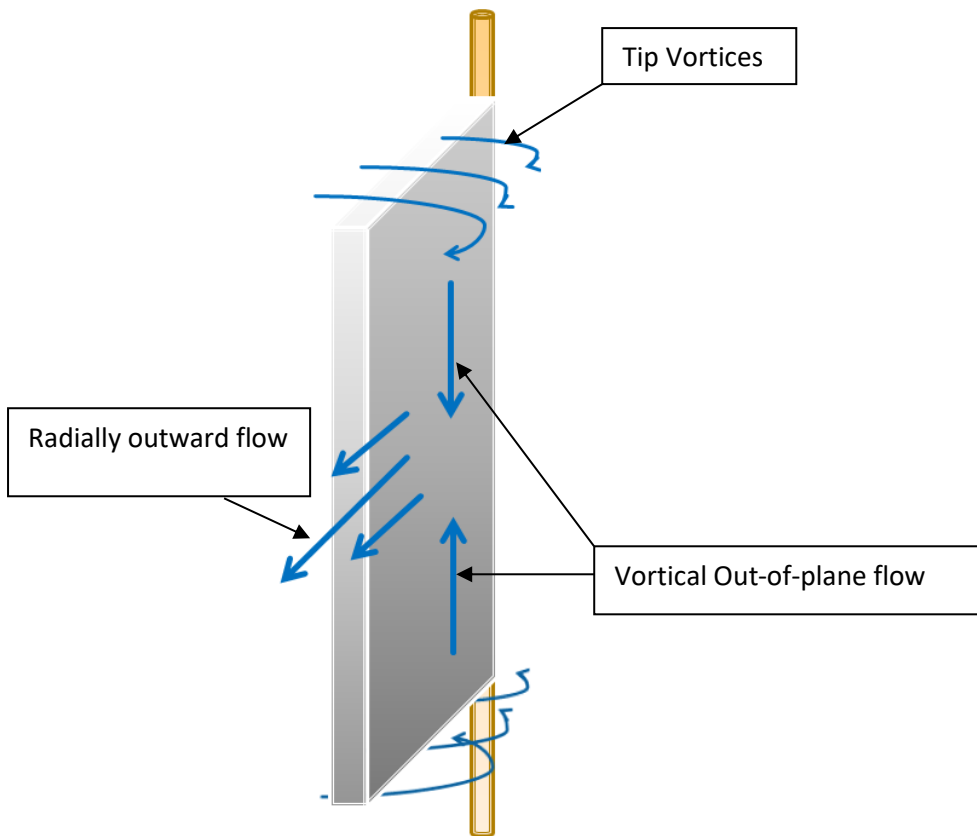


Figure 3.6: Schematic for origin of the source term in the mid-plane. Because of the finite size of the wing, the tip vortices formed will create an outward flow in the mid-plane of the wing

A large source value indicates that 3D effects are very significant in the flow and may be the primary reason for any difference between a 2D and a 3D analysis of flapping flight.

All these plots show the complexity in the wake shed from a wing with simple up-down flapping. 3D vorticity contours presented in the doctoral thesis of Kritivasan Siddharth (Kritivasan, 2016) give a better idea about this.

CHAPTER 4

RESULTS II: FORCE CALCULATION

Even though we have only a 2D velocity field for a primarily 3D flow, certain quantitative estimates can be made by making reasonable approximations. This chapter deals with deriving an estimate of average lift from the 2D velocity field using a control volume approach.

4.1 General Control Volume Analyses

Integral Navier-Stokes equation for a control volume³:

$$\iiint \frac{\partial \mathbf{u}}{\partial t} dV + \iint \bar{\mathbf{u}} \bar{\mathbf{u}} \cdot \bar{\mathbf{n}} dA = - \iint p \bar{\mathbf{n}} dA + \iint \bar{\boldsymbol{\sigma}} \cdot \bar{\mathbf{n}} dA$$

$$\iiint \frac{\partial \mathbf{u}}{\partial t} dV \equiv \text{acceleration term}$$

$$\iint \bar{\mathbf{u}} \bar{\mathbf{u}} \cdot \bar{\mathbf{n}} dA \equiv \text{momentum flux term}$$

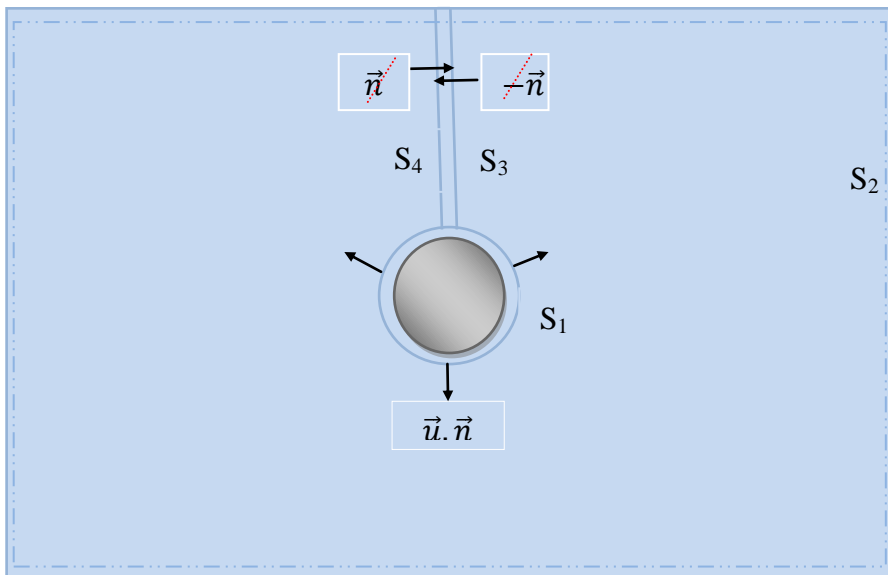


Figure 4.1: Schematic diagram used, to calculate force on a solid body, by the surrounding fluid, using control volume method

³ More details on getting force values from velocity field data can be found at (Noca, 1997). p and $\bar{\boldsymbol{\sigma}}$ have their usual meaning of pressure and shear stress respectively

Total force on body (F_s) = $-\iint p \vec{n} dA + \iint \bar{\sigma} \cdot \vec{n} dA$ on the surface of the body.

(The figure shows a 2D control volume, therefore surface and volume integrals should be replaced with line and surface integrals respectively. No such change is made though as the assumptions and results are general and valid for a 3D case as well)

Considering figure 4.1:

To use the control volume N-S equation, a contour enclosing only the fluid must be drawn.

$$\iiint_{V_f} \frac{\partial \mathbf{u}}{\partial t} dV + \iint_{\substack{S_1+S_2 \\ +S_3+S_4}} \vec{u} \vec{u} \cdot \vec{n} dA = \iint_{\substack{S_1+S_2 \\ +S_3+S_4}} (-p \vec{n} + \bar{\sigma} \cdot \vec{n}) dA$$

$$F_s = -\left(\iint_{S_1} (-p \vec{n} + \bar{\sigma} \cdot \vec{n}) dA \right)$$

$$= -\iiint_{V_f} \frac{\partial \mathbf{u}}{\partial t} dV - \iint_{\substack{S_1+S_2 \\ +S_3+S_4}} \vec{u} \vec{u} \cdot \vec{n} dA - \iint_{S_2+S_3+S_4} (-p \vec{n} + \bar{\sigma} \cdot \vec{n}) dA$$

The contour taken is such that surfaces S_3 and S_4 very close i.e. \vec{u} is same on both surfaces, only the normals to the surfaces are of opposite direction:

$$\iint_{S_3} \vec{u} \vec{u} \cdot \vec{n} dA = \iint_{S_4} \vec{u} \vec{u} \cdot (-\vec{n}) dA$$

Or,

$$\iint_{S_3+S_4} \vec{u} \vec{u} \cdot \vec{n} dA = 0$$

Also, for the same reason

$$\iint_{S_3+S_4} (-p \vec{n} + \bar{\sigma} \cdot \vec{n}) dA = 0$$

$$F_s = -\iiint_{V_f} \frac{\partial \mathbf{u}}{\partial t} dV - \iint_{S_1+S_2} \vec{u} \vec{u} \cdot \vec{n} dA - \iint_{S_2} (-p \vec{n} + \bar{\sigma} \cdot \vec{n}) dA$$

or,

$$F_s = -\iiint_{V_f} \frac{\partial \mathbf{u}}{\partial t} dV - \iint_{S_1+S_2} \vec{u} \vec{u} \cdot \vec{n} dA - \iint_{S_2} (-p \vec{n}) dA$$

Since S_2 is much further away from the boundary layer on the solid and neglecting shear stress.

Specifically for this problem, 2D PIV provides only 2D velocities (u,v) on a plane, instead of a complete 3D velocity description (u,v,w) for the entire volume of fluid surrounding the wings. But even with such limitations, certain quantitative observations can be made nonetheless.⁴

4.2 Control Volume analysis for This Problem

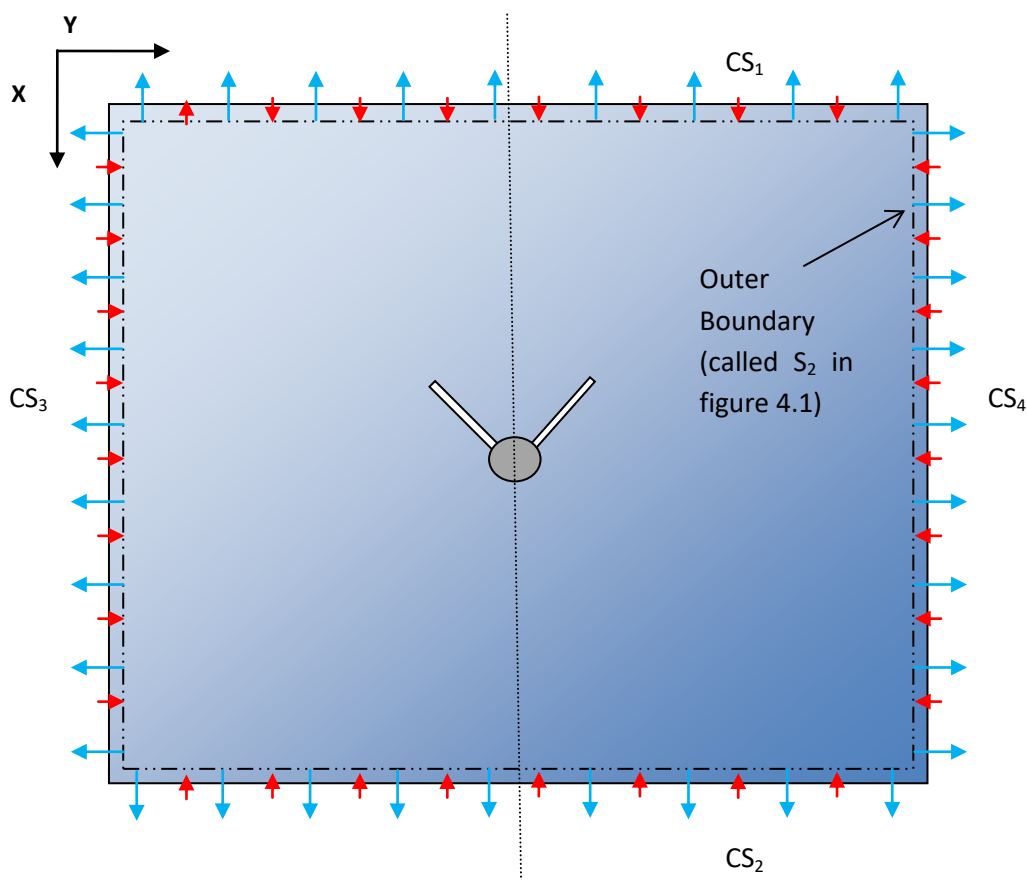


Figure 4.2: Schematic diagram used, to calculate force on a solid flapping body, by the surrounding fluid, using control volume method

Since, $(\vec{u} \cdot \vec{n} = u_{solid} \text{ at each point})$

⁴ Since our fluid control volume also goes around the wing as shown in figure 4.2, it is a function of time. Therefore, there is another term that enters the acceleration term: $\int_{S_b} \vec{u} \vec{u}_s \cdot \vec{n}$ which corresponds to the changing shape of the fluid control volume because of the moving wing. This term goes to zero because of thin wing assumption.

Using the equation obtained in the previous section, for a thin wing (as in our case),

$$\iint_{S_1} \vec{u} \vec{u} \cdot \vec{n} \, dA = 0$$

Considering figure 4.2

$$F_s = - \iiint_{V_f} \frac{\partial \mathbf{u}}{\partial t} \, dV - \iint_{CS_1+CS_2+CS_3+CS_4} \vec{u} \vec{u} \cdot \vec{n} \, dA - \iint_{CS_1+CS_2+CS_3+CS_4} (-p \vec{n}) \, dA$$

This implies that only far-field values of velocities are important for flux calculation.

To calculate lift, only the force in the x-direction matters:

$$\begin{aligned} F_s &= - \iiint_{V_f} \frac{\partial \mathbf{u}_x}{\partial t} \, dV - \left(\iint_{CS_1} u_x u_x \, dA - \iint_{CS_2} u_x u_x \, dA \right) \\ &- \left(\iint_{CS_3} u_x u_y \, dA - \iint_{CS_4} u_x u_y \, dA \right) \\ &- \left(\iint_{CS} u_x u_z \cdot \vec{n} \, dA \right) \quad (\text{Out-of-plane component}) \\ &- \left(\iint_{CS_1} (-p \vec{n}) \, dA - \iint_{CS_2} (-p \vec{n}) \, dA \right) \end{aligned}$$

If the extent of the control volume in the X-direction is such that, the velocity on the top and bottom boundary (CS_1 and CS_2 respectively) is very small, then, since

$$p \sim |u|^2 \sim 0 \quad (\text{Approximation-I})$$

$$\begin{aligned} F_s &= - \iiint_{V_f} \frac{\partial \mathbf{u}_x}{\partial t} \, dV - \left(\iint_{CS_1} u_x u_x \, dA - \iint_{CS_2} u_x u_x \, dA \right) \\ &- \left(\iint_{CS_3} u_x u_y \, dA - \iint_{CS_4} u_x u_y \, dA \right) \\ &- \left(\iint_{CS} u_x u_z \cdot \vec{n} \, dA \right) \end{aligned}$$

Also because, the flapping motion of the body is left-right symmetric, we assume that the flow is also left-right symmetric and only look at one half of the wing. (And also so that we get highly resolved flow for a big area)⁵ (Approximation-II)

For this particular problem, the volume and area considered for integration are of infinitesimal thickness dz as shown in figure 4.3. Hence the lift calculation present in this problem is only for a strip of wing in the mid-plane of the wing of thickness dz .

$$\begin{aligned} \text{Total Lift on mid-plane} = 2 * & \left(- \iiint_{V_f} \frac{\partial u_x}{\partial t} dV - \left(\iint_{CS1} u_x u_x dA - \iint_{CS2} u_x u_x dA \right) \right. \\ & - \left(\iint_{CS4} u_x u_y dA \right) \\ & \left. - \left(\iint_{CS} u_x u_z \cdot \vec{n} dA \right) \right) \end{aligned}$$

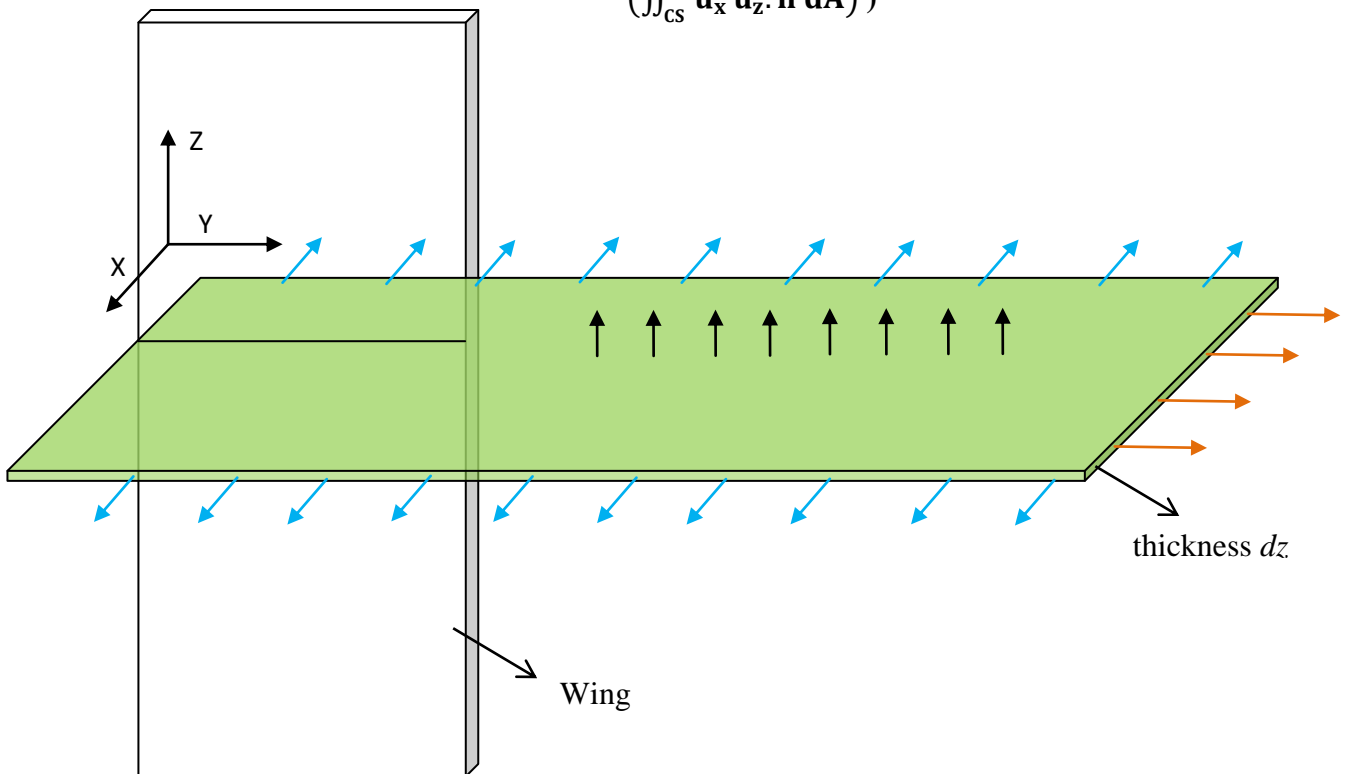


Figure 4.3: Schematic diagram of one-wing and the velocity vectors obtained for the middle cross-section.

⁵ The assumption of left-right asymmetry may not be true instantaneously. But, because average force values have been calculated, this may be a reasonable assumption.

It should be noted that the total lift force on the wing will therefore be a summation/integration, of such strips throughout the chord-wise extent (vertical extent in figure 4.3) of the wing. Now, considering the momentum flux term,

$$-\left(\iint_{CS_1} u_x u_x dA - \iint_{CS_2} u_x u_x dA\right) - \left(\iint_{CS_4} u_x u_y dA\right) - \left(\iint_{CS_{5/6 \text{ out of plane}}} u_x u_z \cdot \vec{n} dA\right),$$

and looking only at $-\left(\iint_{CS} u_x u_z \cdot \vec{n} dA\right)$ contribution:

The flapping motion is up-down symmetric (Following the convention shown in figure 4.4). But, this doesn't necessarily mean that the velocity about the middle plane is symmetric or mirrored. This means, that

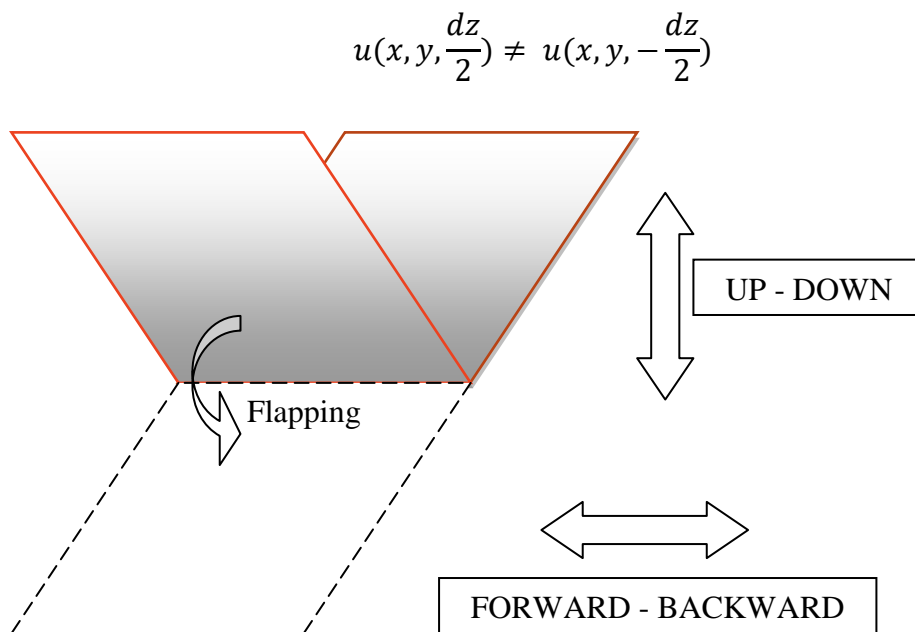


Figure 4.4: Schematic diagram of the flapping body. Forward-backward symmetry breaking has been observed previously in cases with just up-down flapping (Vandenbergh, Zhang, & Childress, 2004)

In other words, even though there is only up-down flapping motion, the fluid can be pushed forward or backward. Spontaneous breaking of forward/backward symmetry in a simple up-down heaving plate has been seen previously (Vandenbergh, Zhang, & Childress, 2004). But, Vandenbergh et al (Vandenbergh, Zhang, & Childress, 2004) from their experiments also noted that, “the wing can move in either direction, with essentially equal probability”.

So, if the contribution of this term is averaged over sufficient number of flapping cycles (to take into account switching from forward inclined jet to a backward one in the same experiment), and also across different experimental realizations (for the cases when there is no such switching in the same experiment, but still there is an out of plane motion set up which can be in either direction with equal probability), it should play no role in the average lift contribution. In other words, there is probably no net forward or backward pushing of the fluid. Therefore, after disregarding this term, (using fig 4.4 for convention)

Total Lift on mid-plane of wing

$$= 2 * (\text{acceleration term} + \text{momentum-flux term 1} + \text{momentum-flux term 2})$$

$$= 2 * \left[- \iiint_{V_f} \frac{\partial u_x}{\partial t} dV - \left(\iint_{CS_{\text{bottom}}} u_x u_x dA - \iint_{CS_{\text{top}}} u_x u_x dA \right) - \left(\iint_{CS_{\text{right}}} u_x u_y dA \right) \right]$$

Using the 2D PIV velocities obtained for the mid-plane of the wing, a reasonable estimate of force can be obtained across AR's. Figure 4.5 shows a representative control volume with respect to the PIV images obtained.

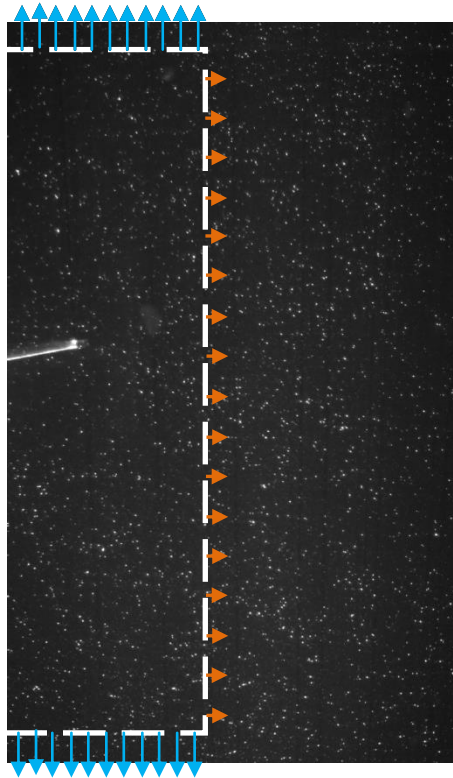


Figure 4.5: Example photo showing control volume overlaid on the PIV image in the present scenario (blue arrows show the showing 2nd term in the above equation)

4.3 Lift Calculation Details

- Backward difference is used to calculate the acceleration term at each point in the volume considered
- Lift calculated is the average value (instantaneous lift values can be seen in appendix 4) for the entire time that PIV vectors have been obtained (usually 30 cycles). It is calculated for only one-wing.
- Lift is normalized by $\frac{1}{2} \rho u_{\text{tip}}^2 * \text{span}$, where u_{tip} is the average tip speed of the wing
 - $u_{\text{tip}} = \frac{2A}{T} * \text{span}$
- Figure 4.6 shows that almost all of the average lift at the end of ~ 30 cycles is because of the in-plane downward pushing of the fluid

$$-\left(\iint_{CS_{\text{bottom}}} \mathbf{u}_x \mathbf{u}_x dA - \iint_{CS_{\text{top}}} \mathbf{u}_x \mathbf{u}_x dA \right) - \left(\iint_{CS_{\text{right}}} \mathbf{u}_x \mathbf{u}_y dA \right)$$

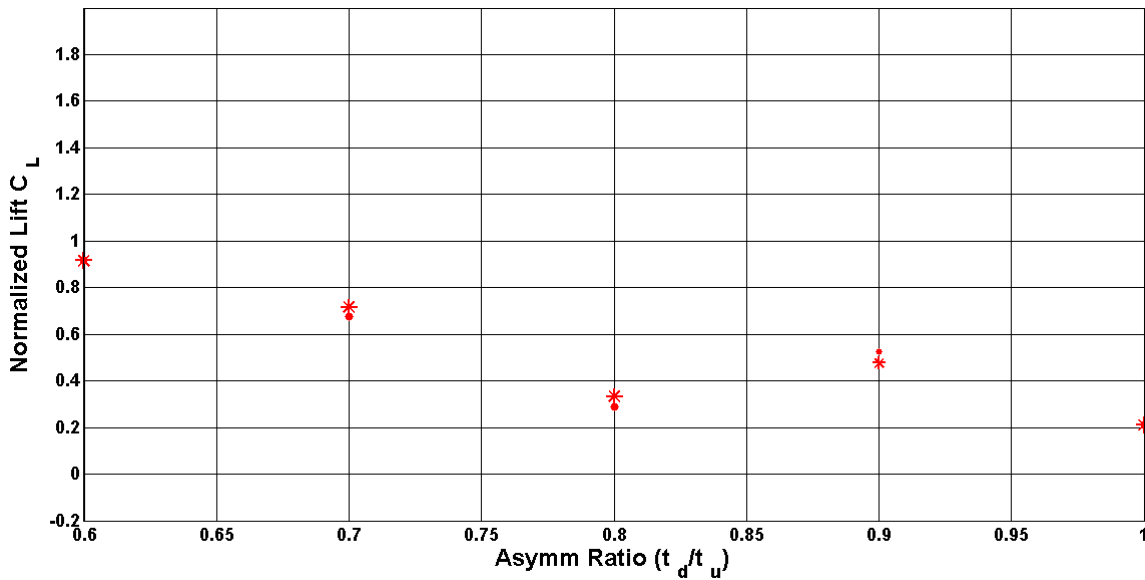
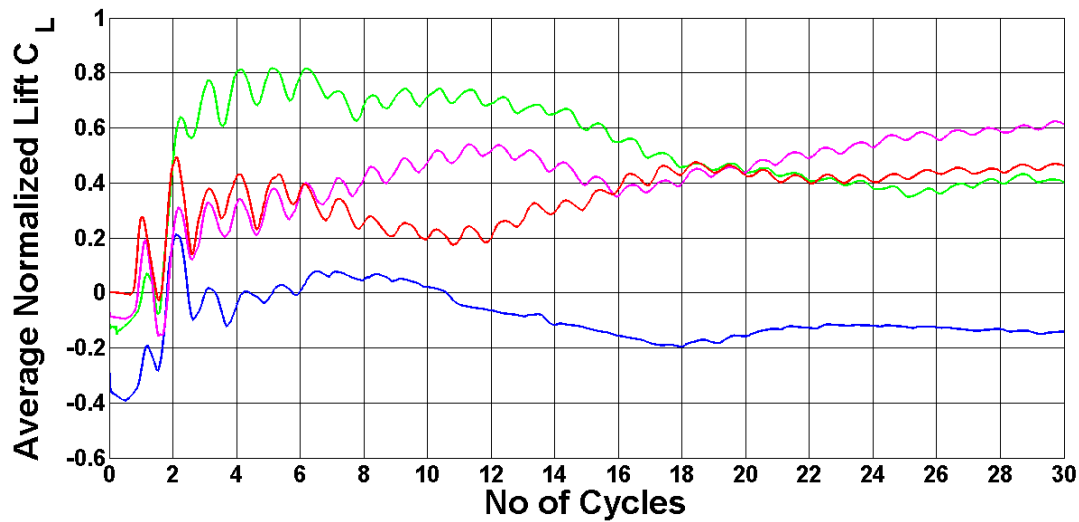


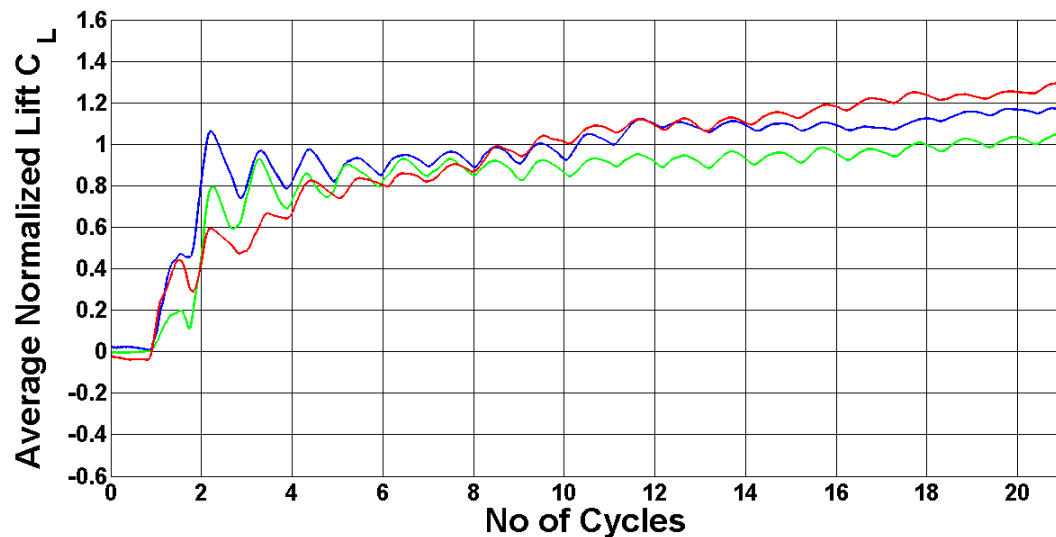
Figure 4.6: Variation of normalized lift on one wing ($\text{Lift}/(\frac{1}{2} \rho u_{\text{tip}}^2 \text{span})$) vs AR for $\text{Re} = 314$; contribution of in-plane momentum flux (stars) against total normalized lift (dots)

4.4 Lift Variation across Flapping Cycles

The “jet meandering” phenomenon (discussed in section 3.2) causes a variation in the momentum flux out of the control volume i.e. this component of the force (which is the major one), is not cycle-wise periodic.



(a)



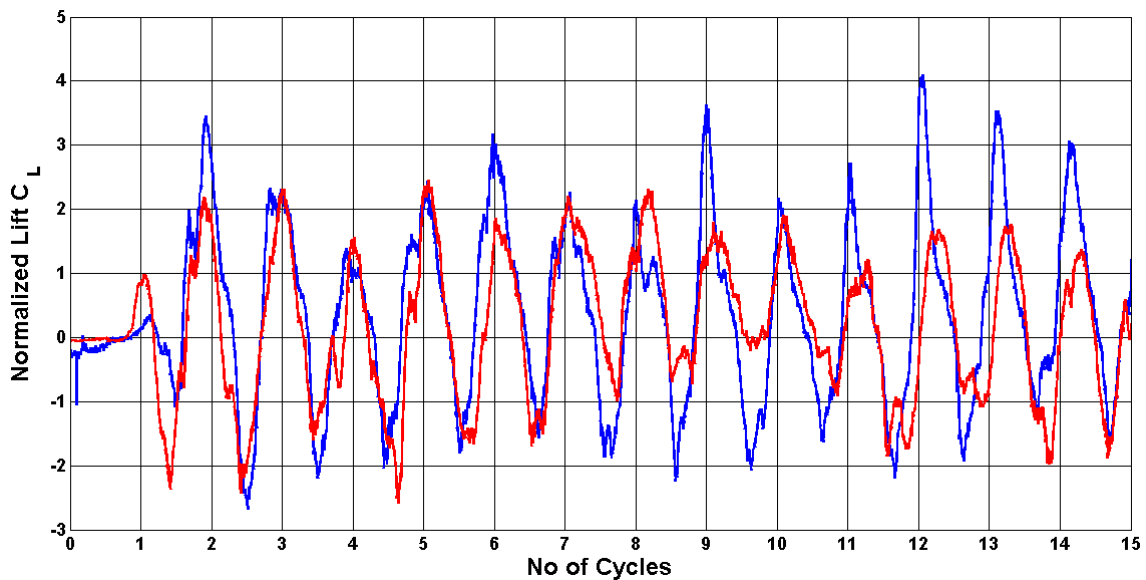
(b)

Figure 4.7: Variation of average normalized in-plane momentum flux for one wing (each point corresponds to average value of lift until that point) over time, for $Re = 314$, (a) $AR=0.9$, (b) $AR=0.6$ for different experiments (each colour represents different runs)

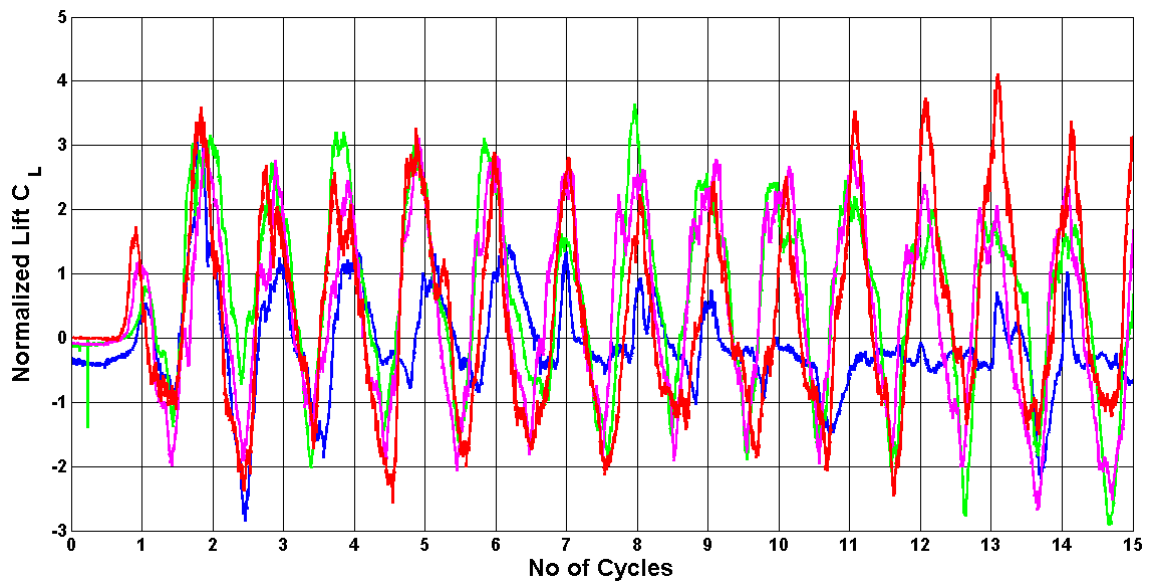
So, averaging for 10 flapping cycles or 20 flapping cycles will give different values of lift. This can be seen clearly in figure 4.7 (a) and (b), which shows how the average force values settle over flapping-cycles for each realization of an experiment.

Averaging for large number of cycles, removes this effect that in-plane jet meandering may have on the control volume estimates, and after ~ 20 cycles most of the realizations seem to settle to some constant value. In most cases, these values coincide, but, one of the experiments in figure 4.7 (a) (blue) seems to be an outlier. This can be seen much more clearly in section 4.7 where comparison across all sets of experiments is shown. If the averaging is done for more cycles, it is possible that, this value may match with the rest.

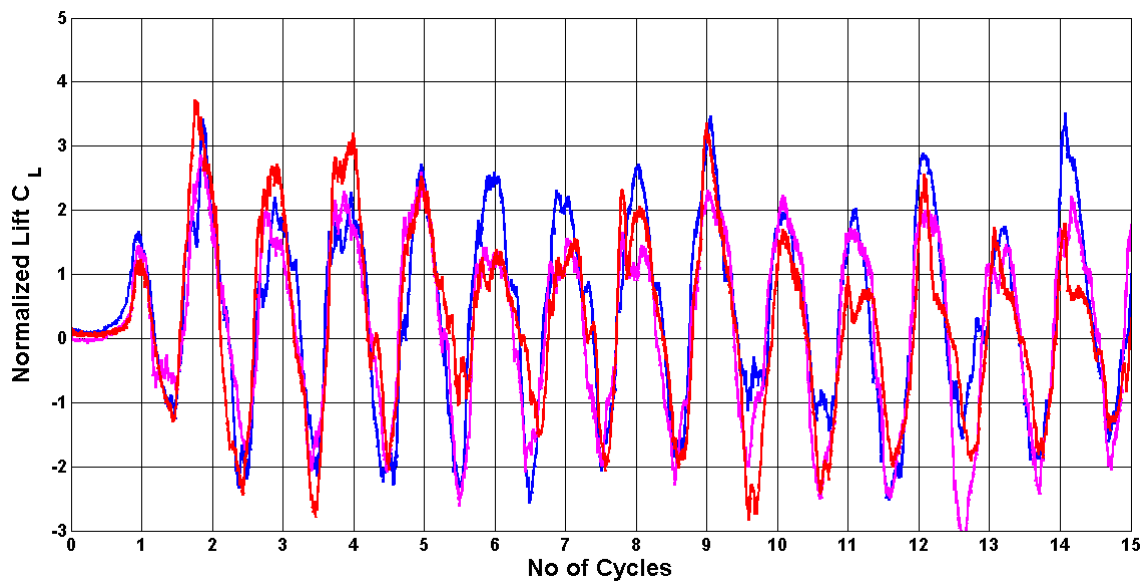
But this outlier, may also be because there is an out of plane motion in the flow field (section 3.3 for more details), which cannot be measured with the 2D PIV done here ($\iint_{CS} u_x u_z \cdot \vec{n} dA$ component of momentum-flux is not calculated in our analysis, see section 4.2). In such a case, as discussed in section 4.2, averaging across different realization of the same experiment will help.



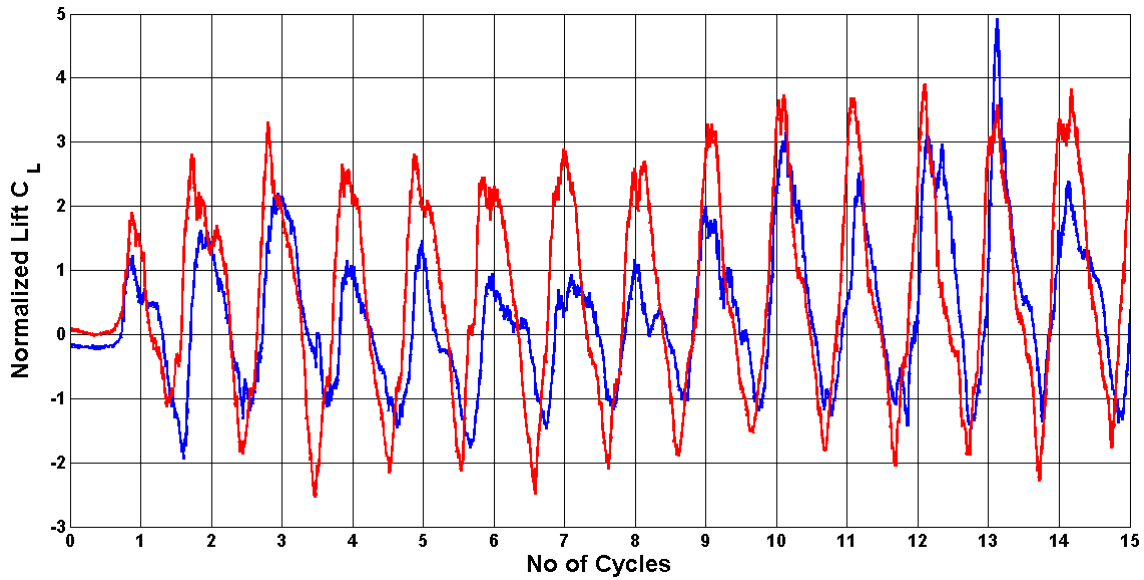
(a)AR = 1



(b) $AR = 0.9$



(c) $AR = 0.8$



(d) AR = 0.7

Figure 4.8: Variation of instantaneous normalized in-plane momentum flux for one wing over time, across different experiments done and asymmetry ratios, for $Re = 314$

Figure 4.8 shows that the momentum-flux component of force is different (instantaneously) across different experiments done as well. This was the difficulty faced in defining repeatability (Refer to section 2.3.1 for flow-field photos). But it can be assumed, as discussed above, that after averaging for enough number of cycles and realizations, what we obtain is the correct representative value.

4.5 Assessment and validity of the lift calculation

Before comparing the actual values obtained across AR's, it is important to recount the limitations of our analysis. The average lift calculated from the mid-plane of the wing may not give the correct estimate of the force on the body because:

- In-plane meandering: As mentioned in section 3.2, the flow produced by the flapping wing meanders in the plane and is not periodically steady. Because of this, a large number of cycles are needed for the average lift to give the correct representative estimate (figure 4.9).
- Out-of-plane flow: At the same time, as shown in section 3.3 and discussed in section 4.2, the flow has a strong out-of-plane flow (refer to appendix 3 for dye photos) which

could instantaneously create a forward-backward asymmetry (figure 4.9 and taking nomenclature from figure 4.4). This will produce a significant UW momentum-flux term, which is not taken into account by our analysis. Averaging for sufficient number of cycles may not be enough as a correction in this case. This is so, because if any directional circulation is set up in the fluid, it may persist for all flapping cycles. In such a case average over multiple runs might solve the problem.

- Finite aspect ratio: By definition, our analysis gives the lift only for the mid-plane of the wing. This means that the total non-dimensional force on the wing:

$$C_{L \text{ actual}} = F\{\text{aspect ratio}\} * C_{L \text{ mid-plane}}$$

Where, $F\{\text{aspect ratio}\}$ is an order one quantity

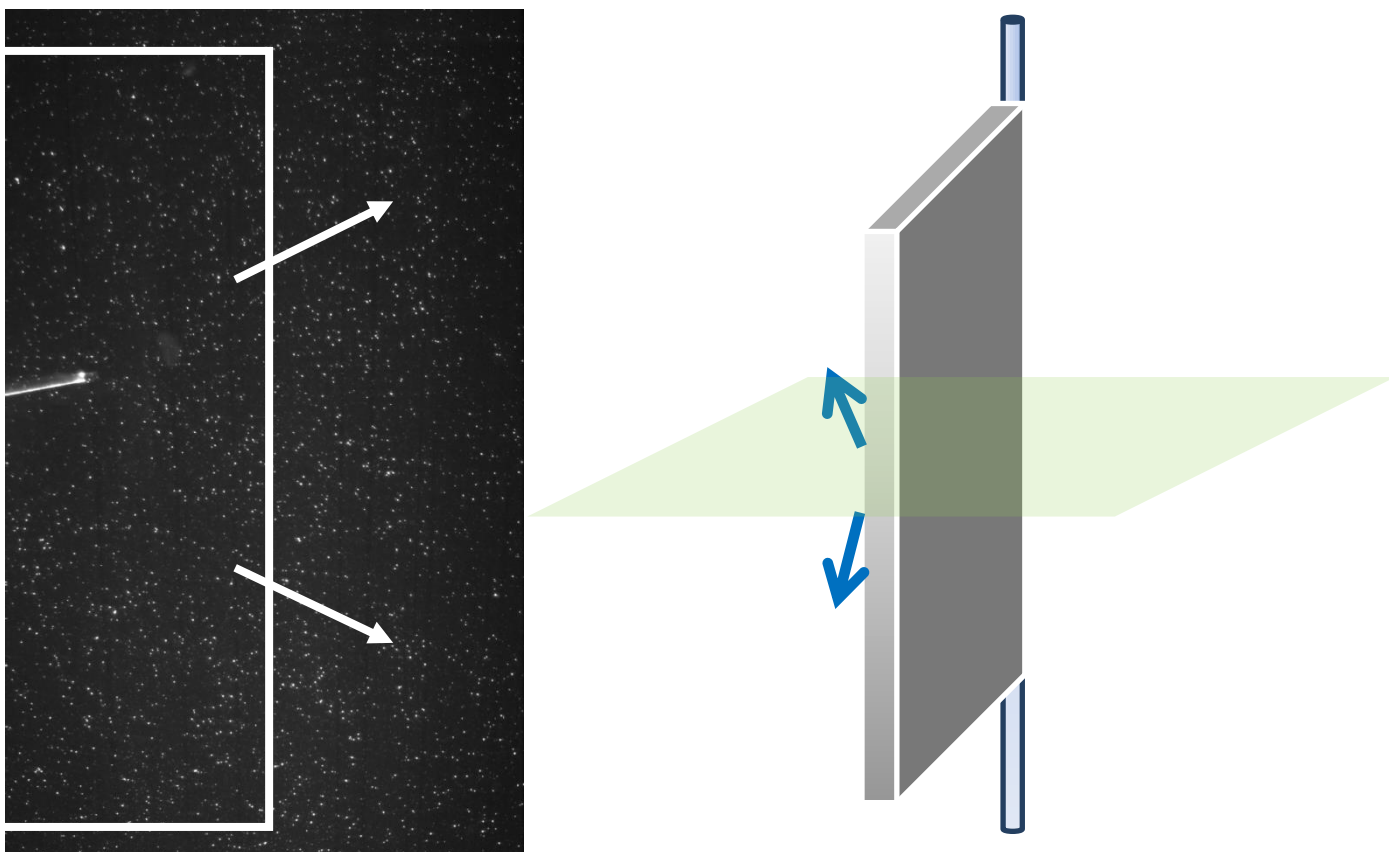


Figure 4.9: Schematic of in-plane meandering (left) and out-of-plane flow (right)

Any variation in the lift, that is calculated for a particular set of parameters across experiments (spread in the data), should be reasonably explained by these reasons.

To conclude, if the averaging is done for enough number of cycles, and across enough experiments, then the value obtained will be the correct estimate of lift for the mid-plane for such a 3D wing configuration.

4.6 Comparison across Re

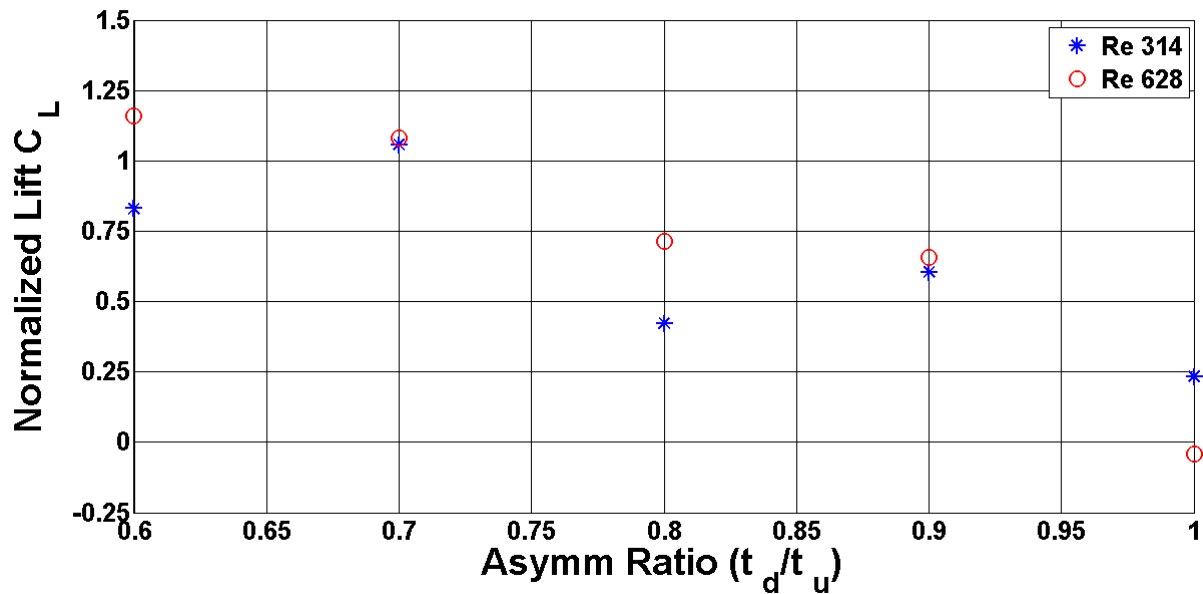


Figure 4.10: Variation normalized lift (for one-wing) vs AR, for different Re; Re = 314 (blue), Re = 628 (red)

Figure 4.10 shows how the normalized lift varies with Reynolds number. Key features to note here are:

- With increase in Reynolds number, there is an increase in lift. But the trend looks more or less similar, and the increase is minimal
- Re 628 experiments are the average forces from 15-45 cycles, while Re 314 case is the average force from 15-30 cycles.

Only one set of experiments was done for Re 628 (no repeatability over different realizations). Therefore any conclusions on variation of lift with Re are limited.

4.7 Comparison across all Experiments and with 2D simulations

This is one of the major quantitative results of this thesis. In Figure 4.11, average normalized lift coefficient is presented for Re 314, for a range of AR's

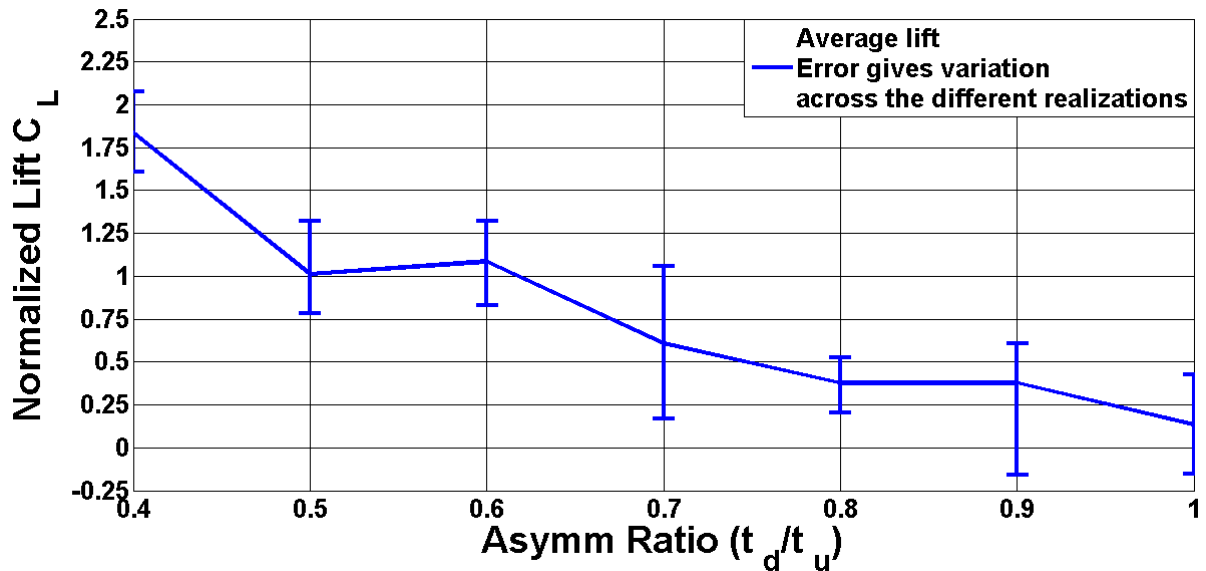


Figure 4.11: Variation of normalized lift (for one wing) vs AR, Re 314; error-bar gives the variation across different realizations. For details of PIV of all the sets of experiments done refer to section 2.4

Key features to note here are:

- There is a general trend of increase in lift with asymmetry ratio as seen from the average lift. Asymmetry ratios below 0.4 weren't investigated because of the limitation in the experimental setup design. But it can be seen from simulation results (Kritivasan, 2016), that there is no change in this trend up till AR = 0.2.
- The outlier for AR = 0.9, as well as the spread in data for AR = 0.7, may be because of not averaging for sufficient number of cycles. Since we're looking at only a portion of the flow, averaging for large number of cycles and realizations is even more relevant, so that the role of any forward-backward asymmetry is minimal (This is discussed in detail in section 4.4)
- No clear local maximum in lift is observed, which is contrary to 2D discrete vortex numerical simulations done by Devranjan (Devranjan, 2009), although the Re in our case is much lower.

- Averaging for more cycles and more experiments for the same parameters, should give better results.
- The resolution of the PIV is different for each set (section 2.4) of experiments done. Moreover, each experiment set looks at slightly different flow region than the other (experimental error). The size of the control volume is also not quite the same in different experiment sets (Although it was checked that this doesn't create a significant difference in force calculations).

Finally, there is some insight gained by comparing 2D Discrete Vortex simulation (original plots shown figure 1.5, and normalized here and shown in figure 4.12) and fig 4.11 and 4.10

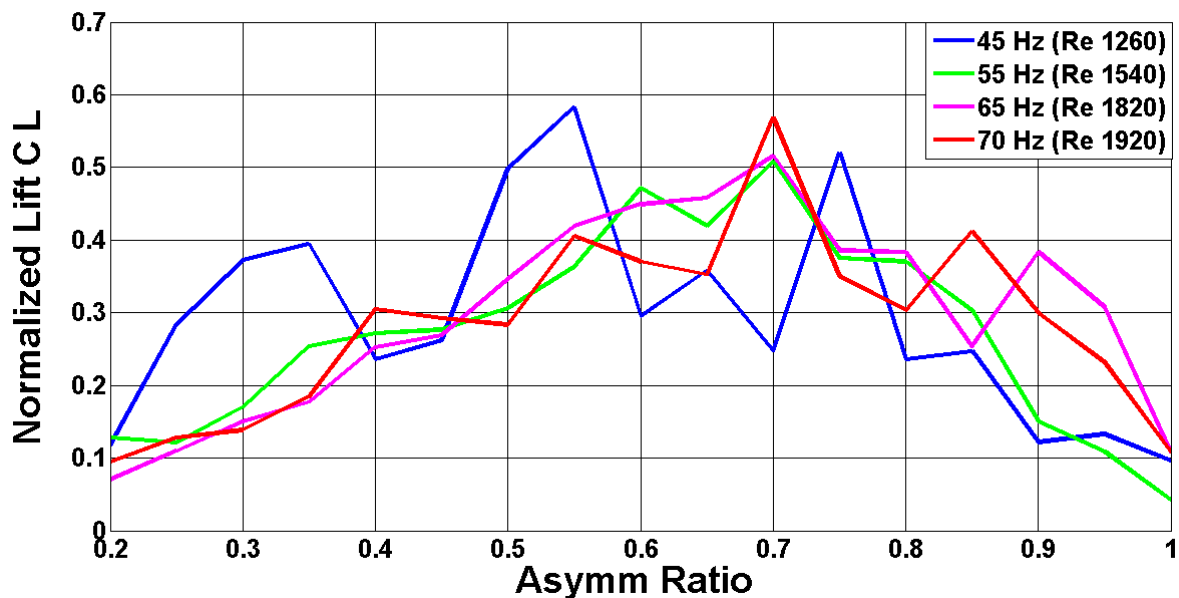


Figure 4.12: Variation of normalized lift vs AR, 2D Discrete Vortex simulations. Data taken from (Devranjan, 2009)

- Unlike a local maxima as seen in 2D simulations (Re 1540 - Re 1920), lift increases continuously in this 3D wing case
- Non-dimensional lift values for both the Re 628 as well as Re 314 case are similar. This is seen in the simulations as well. This shows that there is little or no dependence of normalized lift on Reynolds number
- It can be seen that for the lowest Re considered in simulations (Re 1260, figure 4.12), there is no clear maximum present. Since the Re considered for our experiments is

much lower than this (Re 314, Re 628), it is not altogether surprising that the trend for Re vs AR seen in figure 4.11 and 4.12 is different.

4.8 A note on instantaneous forces

Besides looking at the average value of lift, it is illuminating to look at the instantaneous values of lift as well. Comparing figure 4.13, shown below, and figure 4.8(d), it can be seen that the acceleration term is the major contributor to instantaneous lift.

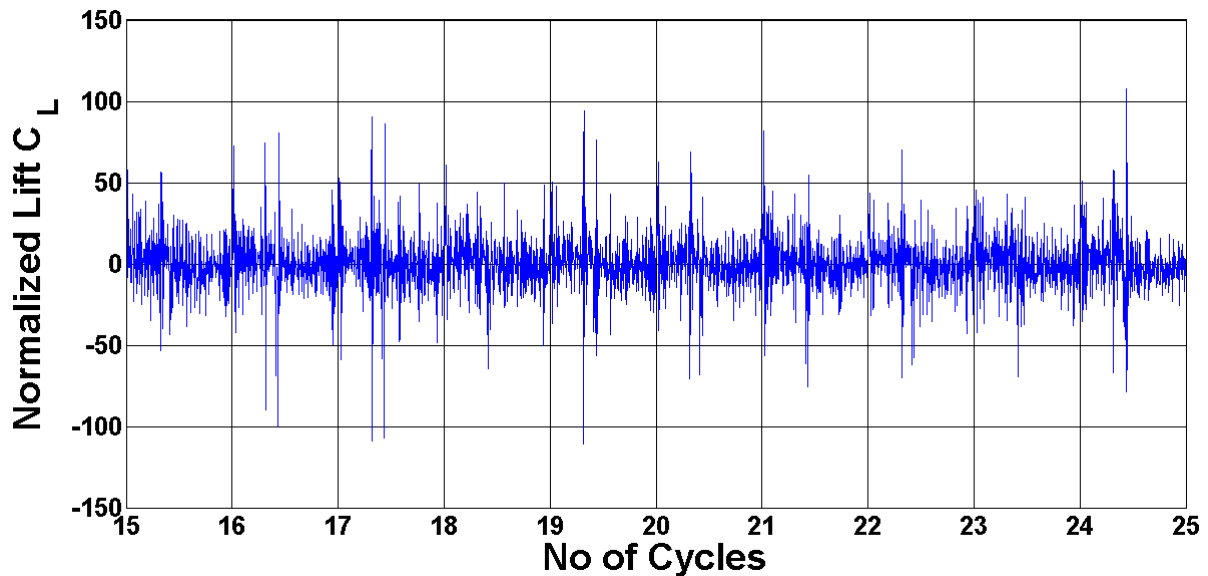


Figure 4.13: Variation of instantaneous normalized acceleration term for one wing over time. Re 314, AR 0.7

The values of instantaneous lift in figure 4.13 are also, two orders of magnitude higher than the average lift values obtained (figure 4.11). This shows that from the point of view of design of an MAV, it is these large instantaneous lift forces that have to be considered. The motor used should be of sufficient power rating to work against the transient peaks in lift forces. Moreover, the importance of studying the time variation of forces is highlighted. But, because of the amount of noise in figure 4.13, a better way to look at the cycle-wise variation of lift is by examining the conditionally averaged force.

- The conditionally averaged force, $F(t)$, is obtained by averaging the instantaneous force, $f(t)$, in the following way:

$$\circ V(x, y, t) = \sum_{n=0}^{30} f(t + n * TimePeriod) / 30$$

- Therefore, from 30 cycles of flapping motion of the wing, we get one representative cycle of the forces.

Figure 4.14 shows the variation of lift (both acceleration and momentum-flux contributions) over one representative conditionally averaged cycle of flow. It is best to look at this along with the velocity profile of the wing, to find out what the role of wing motion may be. Hence, figure 4.14 also shows the angular velocity of the wing (the velocity profile given to the controller).

To reduce noise in the data, the conditionally averaged force for two realizations has been averaged and then a moving average filter (*smooth* function in MATLAB®) has been applied to it. Both plots have been scaled with their respective maximum absolute value for better visualization.

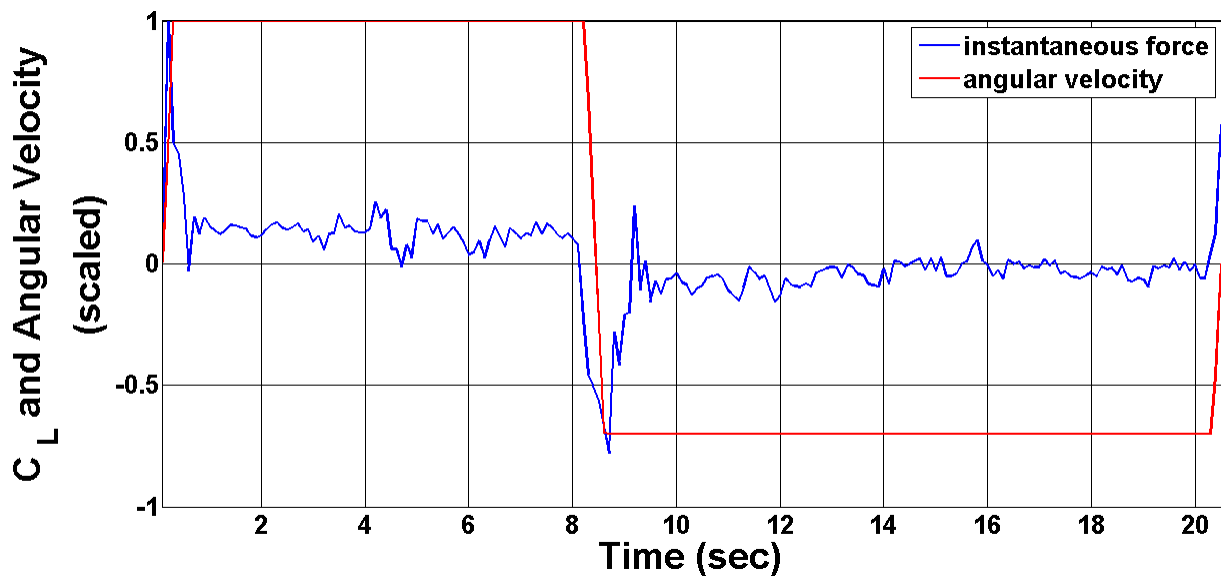


Figure 4.14: Variation of instantaneous normalized force (blue), calculated for one wing (for the mid-plane), and angular velocity (red) for one conditionally averaged cycle. Positive angular velocity represents downstroke. Re 314: AR 0.7

Figure 4.14 clearly shows the following characteristic feature:

- Sudden increase in lift in the beginning: This is probably because of 2 reasons:
 - Added mass effect: The fluid around the wing is also accelerated, along with the wing during this phase.

- Growth of circulation around the wing: This period also corresponds with initial growth of circulation around the wing
- The force reaches its peak value and then drops sharply: This drop has been observed and explained for impulsively started bodies. Koumoutsakos and Leonard (Koumoutsakos & Leonard, 1995) in their numerical simulations calculated the force around an impulsively started cylinder and validated their flow results against flow visualization experiments done by Bouard and Coutanceau (Bouard & Coutanceau, 1980) previously. They observed a similar trend in the drag curve and correlated the steep fall in force (drag on cylinder in their case), with the formation of primary wake vortex of the cylinder as shown in figure 4.15. The cylinder then experiences an increase in force up to a point, with the growth of a secondary vortex, after which the size and strength of this vortex remains the same and the drag curve settles to a steady value. Interestingly, this kind of force variation has been seen in an insect flapping flight study as well. Wang et al (Wang, 2000), simulated the towing on an ellipse, and obtained a similar curve (figure 1.3). The vortex structures formed, although, weren't elucidated or compared with impulsive flow past a cylinder.

It could be argued, looking at figure 4.14, that the drop in lift value can be correlated with the end of the acceleration phase. But, Koumoutsakos et al (Koumoutsakos & Leonard, 1995) started their cylinder at constant velocity, almost instantaneously (the acceleration time was very small) and still observed this trend. Therefore acceleration of the wing, probably, only increases the peak force value and doesn't have an effect on the force dynamics.

- This is followed by a, more or less, constant lift phase before the beginning of the deceleration of wing leading to the start of upstroke.
- During the upstroke, all the above three phases are repeated.

It should be noted from the velocity profile of the wing in figure 4.14, that the acceleration time is very small. With a different wing motion (such as a triangular or a sinusoidal velocity profile), a completely different force curve may be obtained.

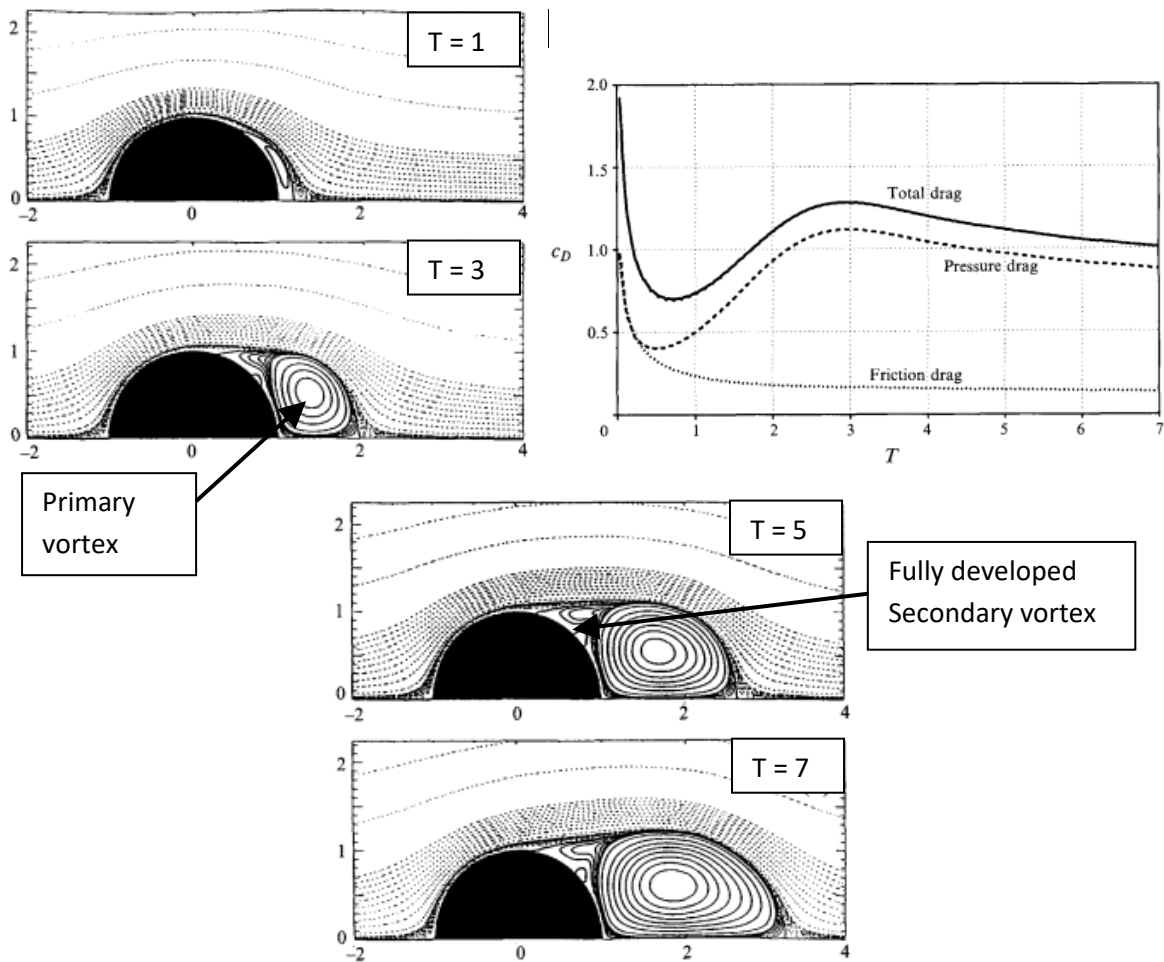


Figure 4.15: Streamline time history (non-dimensional convective time: $T = \frac{U_0 t}{D}$) and evolution of drag force for an impulsively started cylinder (Koumoutsakos & Leonard, 1995). The pressure drag contribution (the shape and magnitude of which is almost the same as total drag) in particular is the one that can be compared directly with the present case (reproduced with permission from author).

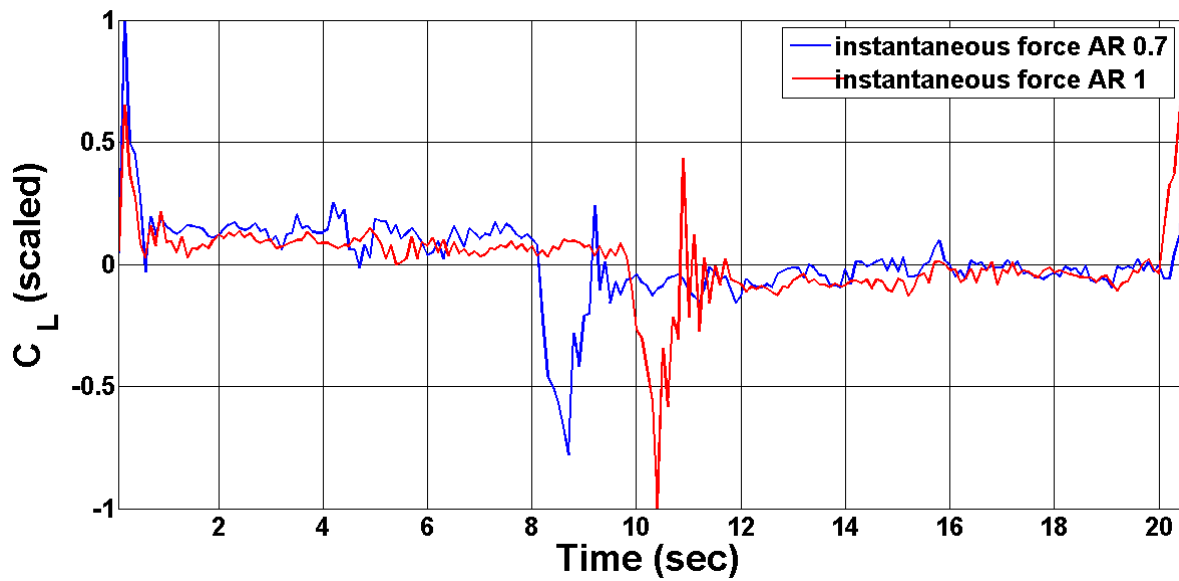


Figure 4.16: Variation of instantaneous normalized force calculated for one wing (for the mid-plane) for one conditionally averaged cycle. Re 314: AR 0.7 (blue) and AR 0.9 (red)

In figure 4.16, the variation of lift for a conditionally averaged flow has been presented for both, an asymmetric, as well as a symmetric flapping case. The force curve shows the shift in the force-peaks which is a clear indication of asymmetry of wing motion, but the major features remain the same

Only limited conclusions, on the time-wise variation of lift forces, can be drawn from the PIV data presented here. This is because of low temporal resolution (200 time snapshots/cycle), and also because only 2D velocity measurements are made for a complex, 3D flow. A better picture of this is obtained, though, by looking at the flow and force results obtained with 3D LBM simulations done in our group (Kritivasan, 2016). Figure 4.17 shows the instantaneous forces from these simulations. The major features of the force-curve in figure 4.17 are captured in our instantaneous estimate of force derived from the conditionally averaged flow.

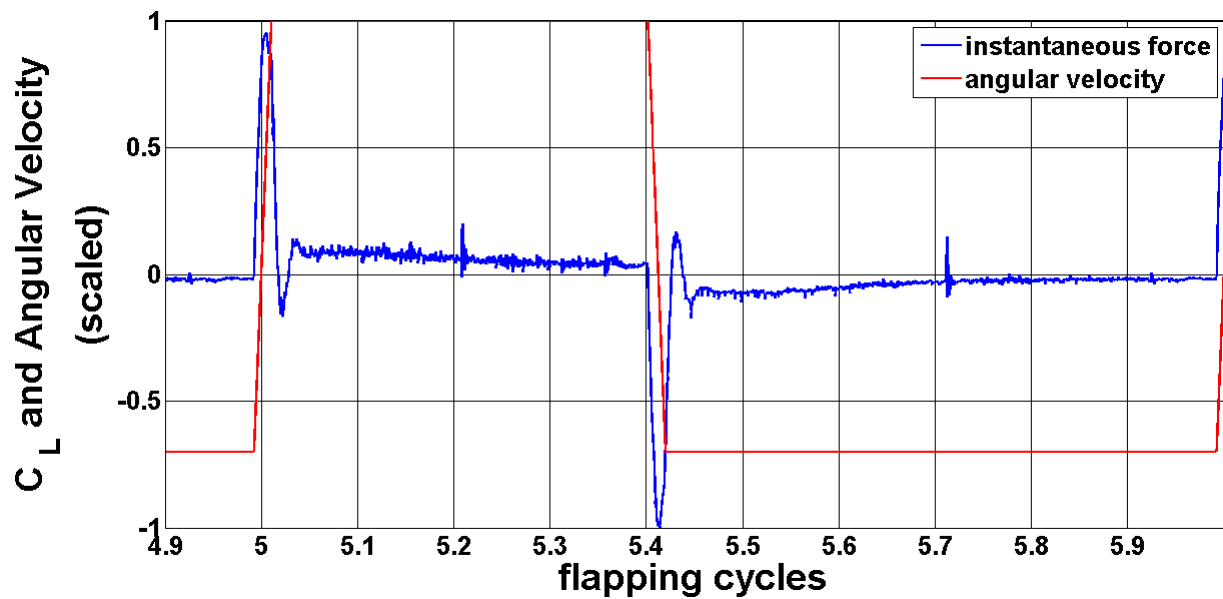


Figure 4.17: Variation of instantaneous normalized force (blue) from 3D lattice Boltzmann simulations (Kritivasan, 2016). Positive angular velocity represents downstroke. Re 314: AR 0.7

A detailed flow and force comparison can be found the doctoral thesis of Kritivasan Siddharth (Kritivasan, 2016).

It should be noted that the flow-field created in our case is 3D (section 3.3) as opposed to the 2D flow past a cylinder. However, the comparisons made in the above discussion are valid because, no 3D effects are observed in the wake of the wing, as can be seen in figure 3.5(a), in the small time-scales related to the varying instantaneous force. Furthermore, the assumptions made for the role of the UW-component of the force (which has been ignored in this analysis) in section 4.2 should hold here as well, as averaging is done over many cycles and for multiple realizations (although, only two here).

CHAPTER 5

CONCLUSIONS AND FUTURE WORK

5.1 Conclusions

The work presented in this thesis confirms that asymmetric flapping does indeed generate lift. Moreover, a simple one degree of freedom model is shown to be able to do this. This work is also used to verify the accuracy of the flow-field and forces calculated using simulations (Kritivasan, 2016). Additionally, the force estimates obtained here, highlight the importance of considering instantaneous forces during MAV design.

It is expected that the average force results obtained from 2D PIV experiments would give a more robust answer (repeatable and with lesser spread) if the averaging is done for more number of cycles. Although this may be the case, it has been shown, somewhat convincingly, that 2D PIV results, can give an estimate of the force on a 3D body.

Beside lift production by up-down asymmetric flapping, this work can also be looked at as a general, and the simplest case for the role of asymmetry in flapping (up-down or forward-backward). Insects and birds in nature, have been seen to have a slightly asymmetric stroke as shown in figure 5.1 and 5.2

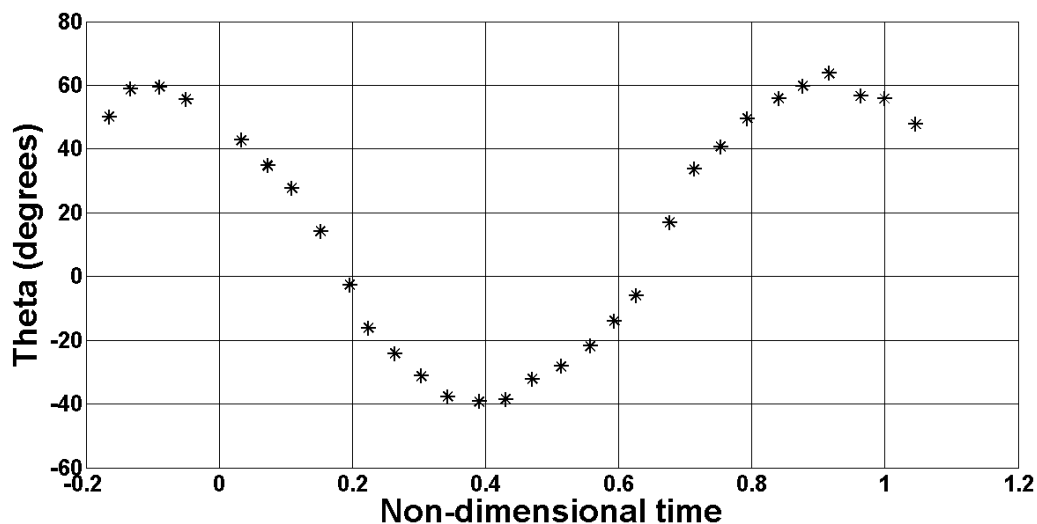


Figure 5.1 Change in angular position of wing in *Diptera* showing asymmetric flapping strokes (minimum around $t=0.4$). Adopted from Ennos (Ennos, 1989)

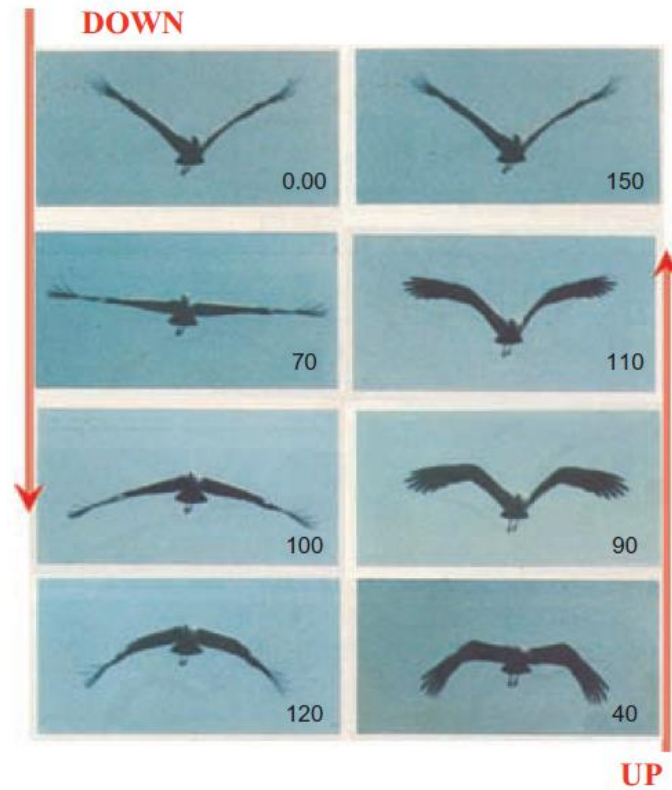


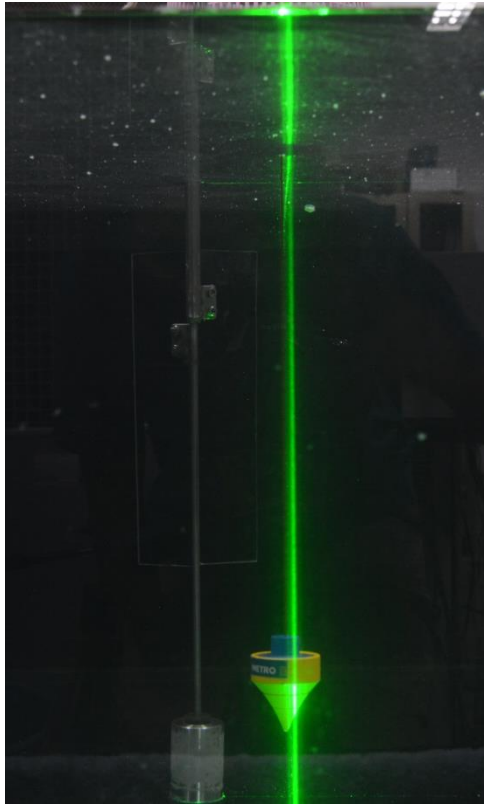
Figure 5.2: Wing motion of a painted stork in flight (The numbers represent the time in milliseconds taken to complete each stroke). Reproduced from (Shreyas, Devranjan, & Sreenivas, Aerodynamics of Bird and Insect flight, 2011). Adopted from (Dhawan, 1991)

5.2 Future Work

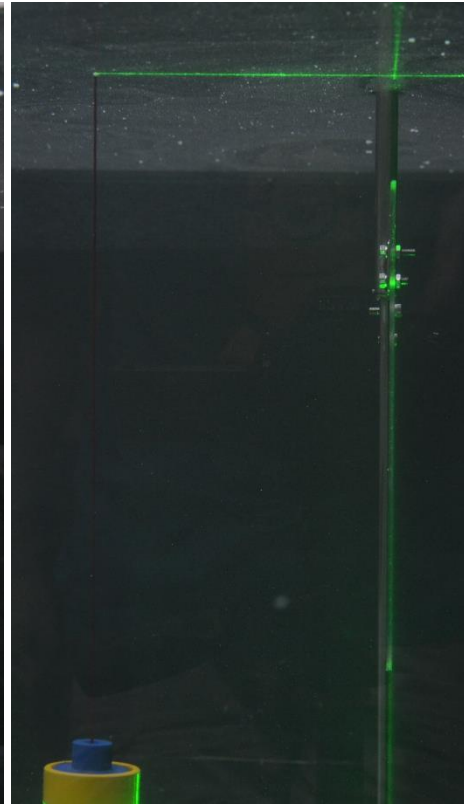
We plan to do more experiments for a range of Re , AR 's, aspect ratios as well as velocity profiles using an in-house 3D, 2-component, PIV mechanism which is close to completion (Singh, 2015). With the help of these future experiments, as well as the results from simulations (Kritivasan, 2016), we hope to bring this problem to a fruitful conclusion.

Appendix 1: how straight is straight?

FRONT VIEW



SIDE VIEW

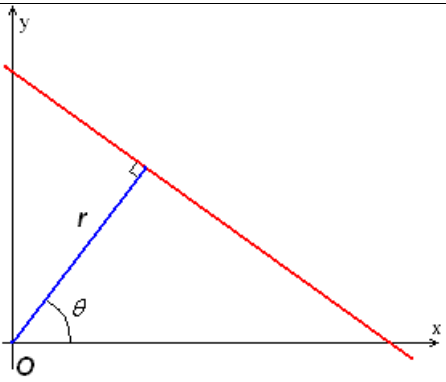


Appendix 2: Hough Transform

The Hough transform⁶ is a technique used to isolate features of a particular shape within an image. The classical Hough transform can be used to detect lines, curves, or other parametrized curves in an image. This technique is used in this thesis, to extract the angle of inclination of the wing with the bottom edge of the image.

Hough transform is essentially a voting algorithm. It creates a polar parameter space:

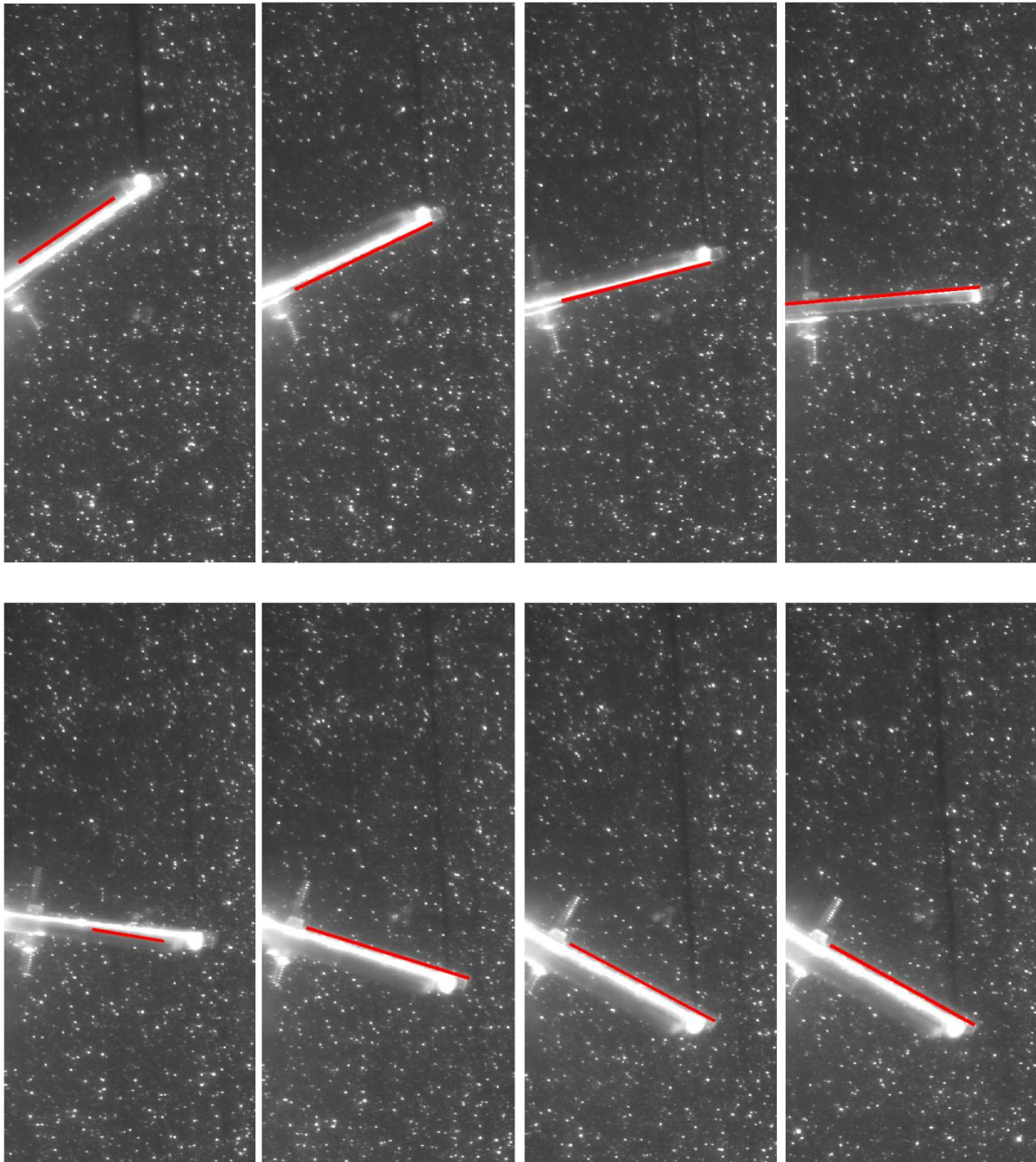
$$r = x \cos \theta + y \sin \theta$$

| | | | | | |
|--|------|------|----|-----|-----|
|  | -90° | -40° | 0° | 40° | 90° |
| 0.1 | | | | | |
| 10 | | | | | |
| 100 | | | | | |

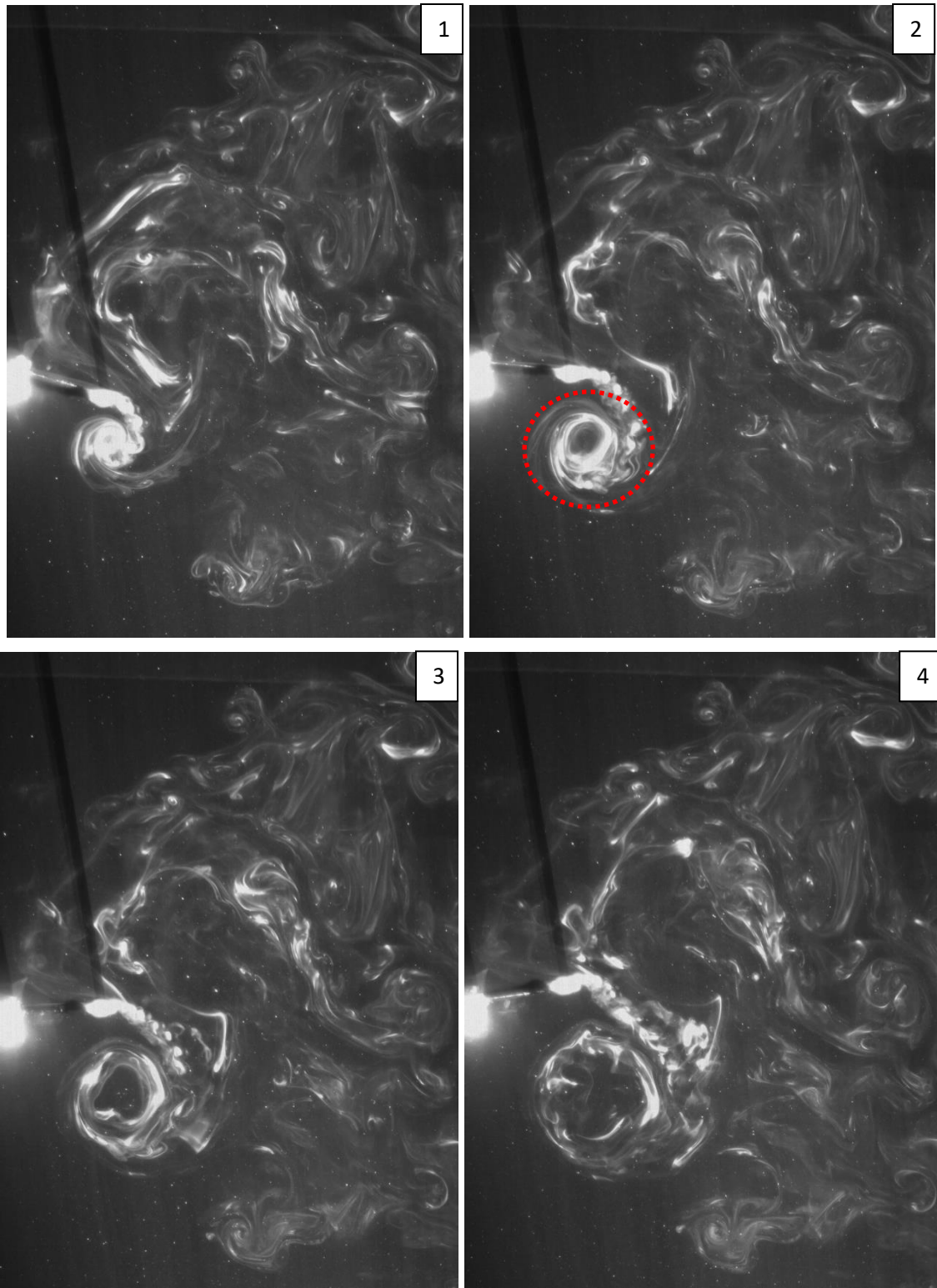
For each point (each bright point for a black-white image) it calculates all possible lines that can pass through it. The corresponding r - θ line gets one vote. At the end, the line with the most votes is chosen. This is the line that is common line to all the bright points

⁶ More details at <http://homepages.inf.ed.ac.uk/rbf/HIPR2/hough.htm>

In this case the wing is tracked as shown:



Appendix 3: Fluorescent dye visualization experiments



The dye was released only in the mid-plane of the wing. A portion of colourless fluid within the vortex implies out-of-plane (3D) flow.

List of References

- Birch, J. M., & Dickinson, M. H. (2001). Spanwise flow and the attachment of leading-edge vortex on insect wings. *Nature*.
- Bouard, R., & Coutanceau, M. (1980). The early stage of development of the wake behind an impulsive started cylinder for $40 \leq Re \leq 10^4$. *Journal of Fluid Mechanics*.
- Devranjan, S. (2009). *Experimental and Numerical Study of Parametric Dependence of Lift in Flapping Flight (Master's thesis)*.
- Dhawan, S. (1991). *Bird Flight*. Indian Academy of Sciences.
- Dickinson, M. H., Lehmann, F.-O., & Sane, S. P. (1999). Wing rotation and aerodynamic basis of insect flight.
- Ellington, C. (1984). The Aerodynamics of Hovering Insect Flight. III. Kinematics. *Philosophical Transaction of the Royal Society B*.
- Ennos, A. (1989). The kinematics and aerodynamics of the free flight of some Diptera. *Journal of Experimental Biology*.
- Heathcote, S., & Gursul, I. (2007). Flexible Flapping Airfoil Propulsion at Low Reynolds Numbers. *AIAA*.
- Koumoutsakos, P., & Leonard, A. (1995). High-resolution simulations of the flow around an impulsively started cylinder using vortex methods. *Journal of Fluid Mechanics*.
- Kritivasan, S. (2016). *(Doctoral Thesis in Preparation)*.
- Lentink, D. (n.d.). *Lentink Lab*. Retrieved from Lentink Lab: <http://lentinklab.stanford.edu/video>
- Miller, L. A., & Peskin, C. S. (2005). A computational fluid dynamics of 'clap and fling' in the smallest insects. *Journal of Experimental Biology*.
- Noca, F. (1997). *On the evaluation of time-dependent fluid dynamic forces on bluff bodies (Doctoral Thesis)*.
- Raffel, M., Willert, C. E., & Kompenhans, J. (1998). *Partical Image Velocimetry: A Practical Guide*.
- Sane, S. P. (2003). The aerodynamics of insect flight. *Journal of Experimental Biology*.
- Shinde, S. Y. (2012). *Creation of an Orderly Jet and Thrust Generation in Quiescent Fluid From an Oscillating Two-dimensional Flexible Foil (Doctoral Thesis)*.
- Shreyas, J. (2005). *Experiments and Numerical Simulations of Flapping Wing Flight (Master's Thesis)*.

- Shreyas, J., Devranjan, S., & Sreenivas, K. (2011). Aerodynamics of Bird and Insect flight. *Journal of the Indian Institute of Science*.
- Singh, K. N. (2015). *3D scanning tomography*.
- Vandenbergh, N., Zhang, J., & Childress, S. (2004). Symmetry breaking leads to forward flight. *Journal of Fluid Mechanics*.
- Wang, Z. J. (2000). Vortex shedding and frequency selection in flapping flight. *Journal of Fluid Mechanics*.
- Wang, Z. J. (2005). Dissecting Insect Flight. *Annual Review of Fluid Mechanics*.
- Weis Fogh, T. (1973). Quick Estimates of Flight Fitness in Hovering Animals, Including Novel Mechanisms for Lift Production. *Journal of Experimental Biology*.